

Chapter 15

Numerical simulations in cosmology

Anatoly Klypin

Astronomy Department, New Mexico State University, Las Cruces, USA

15.1 Synopsis

In section 15.2 we give a short description of different methods used in cosmology. The focus is on the major features of N -body simulations: equations, main numerical techniques, the effects of resolution and methods of halo identification.

In section 15.3 we give a summary of recent results on spatial and velocity biases in cosmological models. Progress in numerical techniques made it possible to simulate halos in large volumes with such an accuracy that halos survive in dense environments of groups and clusters of galaxies. Halos in simulations look like real galaxies, and, thus, can be used to study the biases—differences between galaxies and the dark matter. The biases depend on scale, redshift and circular velocities of selected halos. Two processes seem to define the evolution of the spatial bias: (1) statistical bias and (2) merger bias (merging of galaxies, which happens preferentially in groups, reduces the number of galaxies, but does not affect the clustering of the dark matter). There are two kinds of velocity bias. The pair-wise velocity bias is $b_{12} = 0.6\text{--}0.8$ at $r < 5h^{-1}$ Mpc, $z = 0$. This bias mostly reflects the spatial bias and provides almost no information on the relative velocities of the galaxies and the dark matter. One-point velocity bias is a better measure of the velocities. Inside clusters the galaxies should move slightly faster ($b_v = 1.1\text{--}1.3$) than the dark matter. Qualitatively this result can be understood using the Jeans equations of stellar dynamics. For the standard LCDM model we find that the correlation function and the power spectrum of galaxy-size halos at $z = 0$ are antibiased on scales $r < 5h^{-1}$ Mpc and $k \approx (0.15\text{--}30)h$ Mpc $^{-1}$. In section 15.4 we give a review of the different properties of dark matter halos. Taken from different publications, we present results on (1) the mass and velocity

functions, (2) density and velocity profiles and (3) concentration of halos. The results are not sensitive to the parameters of cosmological models, but formally most of them were derived for popular flat Λ CDM model. In the range of radii $r = (0.005\text{--}1)r_{\text{vir}}$ the density profile for a quiet isolated halo is very accurately approximated by a fit suggested by Moore *et al* (1997): $\rho \propto 1/x^{1.5}(1 + x^{1.5})$, where $x = r/r_s$ and r_s is a characteristic radius. The fit suggested by Navarro *et al* (1995), $\rho \propto 1/x(1 + x)^2$, also gives a very satisfactory approximation with relative errors of about 10% for radii not smaller than 1% of the virial radius. The mass function of $z = 0$ halos with mass below $\approx 10^{13}h^{-1}M_{\odot}$ is approximated by a power law with slope $\alpha = -1.85$. The slope increases with the redshift. The velocity function of halos with $V_{\text{max}} < 500 \text{ km s}^{-1}$ is also a power law with the slope $\beta = -3.8\text{--}4$. The power law extends to halos at least down to 10 km s^{-1} . It is also valid for halos inside larger virialized halos. The concentration of halos depends on mass (more massive halos are less concentrated) and environment, with isolated halos being less concentrated than halos of the same mass inside clusters. Halos have intrinsic scatter of concentration: at 1σ level halos with the same mass have $\Delta(\log c_{\text{vir}}) = 0.18$ or, equivalently, $\Delta V_{\text{max}}/V_{\text{max}} = 0.12$. Velocity anisotropy for both sub-halos and the dark matter is approximated by $\beta(r) = 0.15 + 2x/[x^2 + 4]$, where x is the radius in units of the virial radius.

15.2 Methods

15.2.1 Introduction

Numerical simulations in cosmology have a long history and numerous important applications. The different aspects of the simulations including the history of the subject were reviewed recently by Bertschinger (1998); see also Sellwood (1987) for an older review. More detailed aspects of simulations were discussed by Gelb (1992), Gross (1997) and Kravtsov (1999). Numerical simulations play a very significant role in cosmology. It all started in the 1960s (Aarseth 1963) and 1970s (Peebles 1970, Press and Schechter 1974) with simple N -body problems solved using N -body codes with a few hundred particles. Later the Particle–Particle code (direct summation of all two-body forces) was polished and brought to the state of art (Aarseth 1985). Already those early efforts brought some very valuable fruits. Peebles (1970) studied the collapse of a cloud of particles as a model of cluster formation. The model had 300 points initially distributed within a sphere with no initial velocities. After the collapse and virialization the system looked like a cluster of galaxies. Those early simulations of cluster formation, though producing cluster-like objects, signalled the first problem—a simple model of an initially isolated cloud (top-hat model) results in a density profile for the cluster which is way too steep (power-law slope -4) as compared with real clusters (slope -3). The problem was addressed by Gunn and Gott (1972), who introduced the notion of secondary infall in an effort to solve the problem. Another keystone work of those times is the paper by White (1976), who studied the collapse of 700

particles with different masses. It was shown that if one distributes the mass of a cluster to individual galaxies, two-body scattering will result in mass segregation not compatible with observed clusters. This was another manifestation of the dark matter in clusters. This time it was shown that inside a cluster the dark matter cannot reside inside individual galaxies.

The survival of substructures in galaxy clusters was another problem addressed in that paper. It was found that halos of dark matter, which in real life may represent galaxies, do not survive in the dense environment of galaxy clusters. White and Rees (1978) argued that the real galaxies survive inside clusters because of energy dissipation by the baryonic component. That point of view was accepted for almost 20 years. Only recently was it shown that the energy dissipation probably does not play a dominant role in the survival of galaxies and the dark matter halos are not destroyed by tidal stripping and galaxy–galaxy collisions inside clusters (Klypin *et al* 1999a (KGKK), Ghigna *et al* 2000). The reason why early simulations came to a wrong result was purely numerical: they did not have enough resolution. But 20 years ago it was impossible to make a simulation with sufficient resolution. Even if at that time we had present-day codes, it would have taken about 600 years to make one run.

The generation of initial conditions with a given amplitude and spectrum of fluctuations was a problem for some time. The only correctly simulated spectrum was the flat spectrum which was generated by randomly distributing particles. In order to generate fluctuations with a power spectrum, say $P(k) \propto k^{-1}$, Aarseth *et al* (1979) placed particles along rods. Formally, it generates the spectrum, but the distribution has nothing to do with cosmological fluctuations, which have random phases. Doroshkevich *et al* (1980) and Klypin and Shandarin (1983) were the first to use the Zeldovich (1970) approximation to set the initial conditions. Since then this method has been used to generate initial conditions for arbitrary initial spectrum of perturbations.

Starting in the mid-1980s the field of numerical simulations has blossomed: new numerical techniques have been invented, old ones perfected. The number of publications based on numerical modelling has skyrocketed. To a large extent, this has changed our way of doing cosmology. Instead of questionable assumptions and waving-hands arguments, we have tools for testing our hypotheses and models. As an example, I mention two analytical approximations which were validated by numerical simulations. The importance of both approximations is difficult to overestimate. The first is the Zeldovich approximation, which paved the way for understanding the large-scale structure of the galaxy distribution. The second is the Press and Schechter (1974) approximation, which gives the number of objects formed at different scales at different epochs. Both approximations cannot be formally proved. The Zeldovich approximation is not formally applicable for hierarchical clustering. It must start with smooth perturbations (a truncated spectrum). Nevertheless, numerical simulations have shown that even for the hierarchical clustering the approximation can be used with appropriate filtering of the initial spectrum (see Sahni and Coles (1995) and references

therein). The Press–Schechter approximation is also difficult to justify without numerical simulations. It operates with an initial spectrum and a linear theory, but then (a very long jump) it predicts the number of objects at very nonlinear stage. Because it is not based on any realistic theory of nonlinear evolution, it was an ingenious but wild guess. If anything, the approximation is based on a simple spherical top-hat model. But simulations show that objects do not form in this way—they are formed in a complicated fashion through multiple mergers and accretion along filaments. Still this very simple and very useful prescription gives quite accurate predictions.

This chapter is organized in the following way. Section 15.2 gives the equations which we solve to follow the evolution of initially small fluctuations. Initial conditions are discussed in section 15.3. A brief discussion of different methods is given in section 15.4. The effects of the resolution and some other technical details are also discussed in section 15.5. Identification of halos (‘galaxies’) is discussed in section 15.6.

15.2.2 Equations of evolution of fluctuations in an expanding universe

Usually the problem of the formation and dynamics of cosmological objects is formulated as an N -body problem: for N point-like objects with given initial positions and velocities, find their positions and velocities at any later moment. It should be remembered that this is just a short-cut in our formulation—to make things simple. While it is still mathematically correct in many cases, it does not give a correct explanation for what we do. If we are literally to take this approach, we should follow the motion of zillions of axions, baryons, neutrinos and whatever else our universe is made of. So, what has it to do with the motion of those few millions of particles in our simulations? The correct approach is to start with the Vlasov equation coupled with the Poisson equation and with appropriate initial and boundary conditions. If we neglect the baryonic component, which of course is very interesting, but would complicate our situation even more, the system is described by distribution functions $f_i(\mathbf{x}, \dot{\mathbf{x}}, t)$ which should include all different clustered components i . For a simple CDM model we have only one component (axions or whatever it is). For more complicated Cold plus Hot Dark Matter (CHDM) with several different types of neutrinos the system includes one distribution function for the cold component and one distribution function for each type of neutrino (Klypin *et al* 1993). In the comoving coordinates \mathbf{x} , the equations for the evolution of f_i are:

$$\frac{\partial f_i}{\partial t} + \dot{\mathbf{x}} \frac{\partial f_i}{\partial \mathbf{x}} - \nabla \phi \frac{\partial f_i}{\partial \mathbf{p}} = 0, \quad \mathbf{p} = a^2 \dot{\mathbf{x}}, \quad (15.1)$$

$$\nabla^2 \phi = 4\pi G a^2 (\rho_{\text{dm}}(\mathbf{x}, t) - \langle \rho_{\text{dm}}(t) \rangle) = 4\pi G a^2 \Omega_{\text{dm}} \delta_{\text{dm}} \rho_{\text{cr}}, \quad (15.2)$$

$$\delta_{\text{dm}}(\mathbf{x}, t) = (\rho_{\text{dm}} - \langle \rho_{\text{dm}} \rangle) / \langle \rho_{\text{dm}} \rangle, \quad (15.3)$$

$$\rho_{\text{dm}}(\mathbf{x}, t) = a^{-3} \sum_i m_i \int d^3 \mathbf{p} f_i(\mathbf{x}, \dot{\mathbf{x}}, t). \quad (15.4)$$

Here $a = (1 + z)^{-1}$ is the expansion parameter, $\mathbf{p} = a^2 \dot{\mathbf{x}}$ is the momentum, Ω_{dm} is the contribution of the clustered dark matter to the mean density of the universe, m_i is the mass of a particle of the i th component of the dark matter. The solution of the Vlasov equation can be written in terms of equations for the characteristics, which *look* like equations of particle motion:

$$\frac{d\mathbf{p}}{da} = -\frac{\nabla\phi}{\dot{a}}, \quad \frac{d\mathbf{v}}{dt} + 2\frac{\dot{a}}{a}\mathbf{v} = -\frac{\nabla\phi'}{a^3}, \quad (15.5)$$

$$\frac{d\mathbf{x}}{da} = \frac{\mathbf{p}}{\dot{a}a^2}, \quad \frac{d\mathbf{x}}{dt} = \mathbf{v}, \quad (15.6)$$

$$\nabla^2\phi = 4\pi G\Omega_0\delta_{\text{dm}}\rho_{\text{cr},0}/a, \quad \phi' = a\phi, \quad (15.7)$$

$$\dot{a} = H_0\sqrt{1 + \Omega_0\left(\frac{1}{a} - 1\right) + \Omega_\Lambda(a^2 - 1)}. \quad (15.8)$$

In these equations $\rho_{\text{cr},0}$ is the critical density at $z = 0$; Ω_0 , and $\Omega_{\Lambda,0}$, are the density of the matter and of the cosmological constant in units of the critical density at $z = 0$.

The distribution function f_i is constant along each characteristic. This property should be preserved by numerical simulations. The complete set of characteristics coming through every point in the phase space is equivalent to the Vlasov equation. We cannot have the complete (infinite) set, but we can follow the evolution of the system (with some accuracy), if we select a representative sample of characteristics. One way of doing this would be to split the initial phase space into small domains, to take only one characteristic as being representative of each volume element, and to follow the evolution of the system of ‘particles’ in a self-consistent way. In models with one ‘cold’ component of clustering dark matter (like the CDM or Λ CDM models) the initial velocity is a unique function of the coordinates (only the ‘Zeldovich’ part is present, no thermal velocities). This means that we need only to split the coordinate space, not the velocity space. For complicated models with a significant thermal component, the distribution in the full phase space should be taken into account. Depending on what we are interested in, we might split the initial space into equal-size boxes (a typical set-up for PM or P³M simulations) or we could divide some area of interest (say, where a cluster will form) into smaller boxes, and use much bigger boxes outside the area (to mimic the gravitational forces of the outside material). In any case, the mass assigned to a ‘particle’ is equal to the mass of the domain it represents. Now we can think of the ‘particle’ either as a small box, which moves with the flow but does not change its original shape, or as a point-like particle. Both presentations are used in simulations. None is superior to another.

There are different forms of final equations. Mathematically they are all equivalent but computationally there are very significant differences. There are considerations, which may affect the choice of a particular form of the equations. Any numerical method gives more accurate results for a variable, which changes slowly with time. For example, for the gravitational potential we can choose either

ϕ or ϕ' . At early stages of evolution perturbations still grow almost linearly. In this case we expect that $\delta_{\text{dm}} \propto a$, $\phi \approx \text{constant}$ and $\phi' \approx a$. Thus, ϕ can be a better choice because it does not change. This is especially helpful, if the code uses the gravitational potential from a previous moment of time as an initial ‘guess’ for the current moment, as happens in the case of the ART code. In any case, it is better to have a variable which does not change much. For equations of motion we can choose, for example, either the first equations in (15.5)–(15.6) or the second equations. If we choose the ‘momentum’ $p = a^2 \dot{x}$ as the effective velocity and take the expansion parameter a as the time variable, then for linear growth we expect the change of coordinates per each step to be constant: $\Delta x \propto \Delta a$. Numerical integration schemes should not have a problem with this type of growth. For the t and v variables, the rate of change is more complicated: $\Delta x \propto a^{-1/2} \Delta t$, which may produce some errors at small expansion parameters. The choice of variables may affect the accuracy of the solution even at a very nonlinear stage of the evolution as was argued by Quinn *et al* (1997).

15.2.3 Initial conditions

15.2.3.1 The Zeldovich approximation

The Zeldovich approximation is commonly used to set initial conditions. The approximation is valid in mildly nonlinear regimes and is much superior to the linear approximation. We slightly rewrite the original version of the approximation to incorporate cases (like CHDM) when the growth rates $g(t)$ depends on the wavelength of the perturbation $|\mathbf{k}|$. In the Zeldovich approximation the comoving and Lagrangian coordinates are related in the following way:

$$\mathbf{x} = \mathbf{q} - \alpha \sum_{\mathbf{k}} g_{|\mathbf{k}|}(t) \mathbf{S}_{|\mathbf{k}|}(\mathbf{q}), \quad \mathbf{p} = -\alpha a^2 \sum_{\mathbf{k}} g_{|\mathbf{k}|}(t) \left(\frac{\dot{g}_{|\mathbf{k}|}}{g_{|\mathbf{k}|}} \right) \mathbf{S}_{|\mathbf{k}|}(\mathbf{q}), \quad (15.9)$$

where the displacement vector \mathbf{S} is related to the velocity potential Φ and the power spectrum of fluctuations $P(|\mathbf{k}|)$:

$$\mathbf{S}_{|\mathbf{k}|}(\mathbf{q}) = \nabla_{\mathbf{q}} \Phi_{|\mathbf{k}|}(\mathbf{q}), \quad \Phi_{|\mathbf{k}|} = \sum_{\mathbf{k}} a_{\mathbf{k}} \cos(\mathbf{k}\mathbf{q}) + b_{\mathbf{k}} \sin(\mathbf{k}\mathbf{q}), \quad (15.10)$$

where a and b are Gaussian random numbers with mean zero and dispersion $\sigma^2 = P(k)/k^4$:

$$a_{\mathbf{k}} = \sqrt{P(|\mathbf{k}|)} \frac{\text{Gauss}(0, 1)}{|\mathbf{k}|^2}, \quad b_{\mathbf{k}} = \sqrt{P(|\mathbf{k}|)} \frac{\text{Gauss}(0, 1)}{|\mathbf{k}|^2}. \quad (15.11)$$

The parameter α , together with the power spectrum $P(k)$, define the normalization of the fluctuations.

In order to set the initial conditions, we choose the size of the computational box L and the number of particles N^3 . The phase space is divided into small equal cubes of size $2\pi/L$. Each cube is centred on a harmonic $\mathbf{k} = 2\pi/L \times \{i, j, k\}$, where $\{i, j, k\}$ are integer numbers with limits from zero to $N/2$. We realize the spectrum of perturbations $a_{\mathbf{k}}$ and $b_{\mathbf{k}}$, and find the displacement and the momenta of particles with $\mathbf{q} = L/N \times \{i, j, k\}$ using equation (15.9). Here $i, j, k = 1, N$.

15.2.3.2 Power spectrum

There are approximations of the power spectrum $P(k)$ for a wide range of cosmological models. The publicly available COSMICS code (Bertschinger 1996) gives accurate approximations for the power spectrum. Here we follow Klypin and Holtzman (1997) who give the following fitting formula:

$$P(k) = \frac{k^n}{(1 + P_2 k^{1/2} + P_3 k + P_4 k^{3/2} + P_5 k^2)^{2P_6}}. \quad (15.12)$$

The coefficients P_i are presented by Klypin and Holtzman (1997) for a variety of models. A comparison of some of the power spectra with the results from COSMICS (Bertschinger 1996) indicate that the errors of the fits are smaller than 5%. Table 15.1 gives the parameters of the fits for some popular models. The power spectrum of cosmological models is often approximated using a fitting formula given by Bardeen *et al* (1986, BBKS):

$$P(k) = k^n T^2(k),$$

$$T(k) = \frac{\ln(1 + 2.34q)}{2.34q} [1 + 3.89q + (16.1q)^2 + (5.4q)^3 + (6.71q)^4]^{-1/4}, \quad (15.13)$$

where $q = k/(\Omega_0 h^2 \text{ Mpc}^{-1})$. Unfortunately, the accuracy of this approximation is not great and it should not be used for accurate simulations. We find that the following approximation, which is a combination of a slightly modified BBKS fit and the Hu and Sugiyama (1996) scaling with the amount of baryons, provides errors in the power spectrum which are less than 5% for the range of wavenumbers $k = (10^{-4} - 40)h \text{ Mpc}^{-1}$ and for $\Omega_b/\Omega_0 < 0.1$:

$$P(k) = k^n T^2(k),$$

$$T(k) = \frac{\ln(1 + 2.34q)}{2.34q} [1 + 13q + (10.5q)^2 + (10.4q)^3 + (6.51q)^4]^{-1/4},$$

$$q = \frac{k(T_{\text{CMB}}/2.7 \text{ K})^2}{\Omega_0 h^2 \alpha^{1/2} (1 - \Omega_b/\Omega_0)^{0.60}}, \quad \alpha = a_1^{-\Omega_b/\Omega_0} a_2^{-(\Omega_b/\Omega_0)^3},$$

$$a_1 = (46.9\Omega_0 h^2)^{0.670} [1 + (32.1\Omega_0 h^2)^{-0.532}],$$

$$a_2 = (12\Omega_0 h^2)^{0.424} [1 + (45\Omega_0 h^2)^{-0.582}]. \quad (15.14)$$

Table 15.1. Approximations of the power spectra.

Ω_0	Ω_{bar}	h	P_2	P_3	P_4	P_5	P_6
0.3	0.035	0.60	-1.7550E+00	6.0379E+01	2.2603E+02	5.6423E+02	9.3801E-01
0.3	0.030	0.65	-1.6481E+00	5.3669E+01	1.6171E+02	4.1616E+02	9.3493E-01
0.3	0.026	0.70	-1.5598E+00	4.7986E+01	1.1777E+02	3.2192E+02	9.3030E-01
1.0	0.050	0.50	-1.1420E+00	2.9507E+01	4.1674E+01	1.1704E+02	9.2110E-01
1.0	0.100	0.50	-1.3275E+00	3.0152E+01	5.5515E+01	1.2193E+02	9.2847E-01

15.2.3.3 Multiple masses: high resolution for a small region

In many cases we would like to set initial conditions in such a way that inside some specific region(s) there are more particles and the spectrum is better resolved. A rigorous but complicated approach for the problem is described by Bertschinger (2001). Here I give a simplified prescription. The procedure has two steps. First, we run a low-resolution simulation which has a sufficiently large volume to include the effects of the environment. For this run all the particles have the same mass. A halo is picked for rerunning with high resolution. Second, using particles of the halo, we identify a region in the Lagrangian (initial) space, where the resolution should be increased. We add high-frequency harmonics, which are not present in the low-resolution run. We then add the contributions from all the harmonics and get initial displacements and momenta (equation (15.9)). Let us be more specific. In order to add the new harmonics, we must specify (1) how we divide the phase space and place the harmonics and (2) how we sum the contributions of the harmonics.

The simplest way is to divide the phase space into many small boxes of size $2\pi/L$, where L is the box size. This is the same division, which we use to set the low-resolution run. But now we extend it to very high frequencies up to $2\pi/L \times N/2$, where N is the new effective number of particles. For example, we used $N = 64$ for the low-resolution run. For a high-resolution run we may choose $N = 1024$. Simply replace the value and run the code again. Of course, we really cannot do it because it would generate too many particles. Instead, in some regions, where the resolution should not be high, we combine particles together (by taking average coordinates and average velocities) and replace many small-mass particles with fewer larger ones. The top panel in figure 15.1 gives an example of mass refinement. Note that we try to avoid jumps that are too large in the mass resolution by creating layers of particles of increasing mass.

This approach is correct and relatively simple. It may seem that it takes too much CPU time to obtain the initial conditions. In practice, CPU time is not much of an issue because initial conditions are generated only once and it takes only a few CPU hours even for a 1024^3 mesh. For most applications 1024^3 particles is more than enough. The problem arises when we want to have more

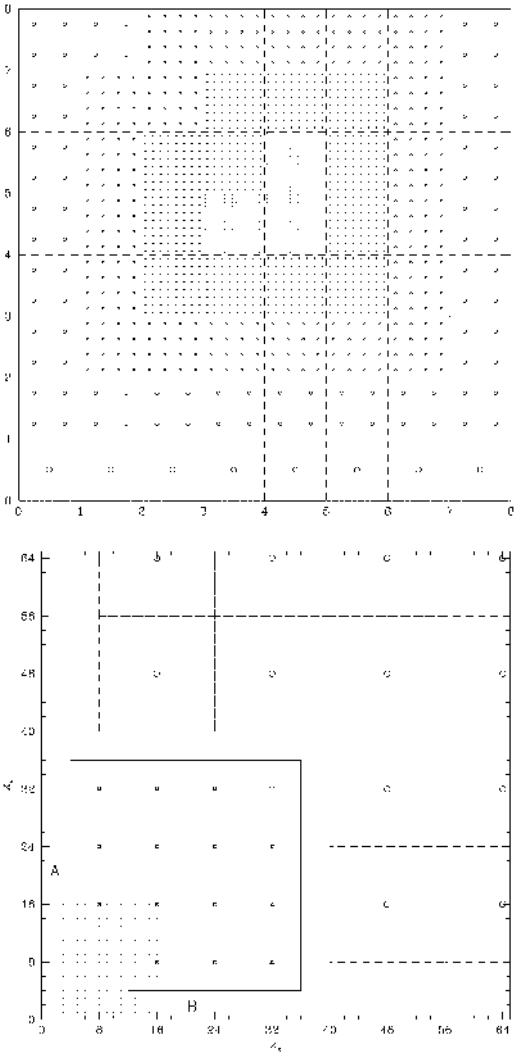


Figure 15.1. An example of the construction of mass refinement in real space (top) and in phase space (bottom). In real space (*top panel*) three central blocks of particles were marked for highest mass resolution. Each block produces 16^2 of smallest particles. Adjacent blocks get one step lower resolution and produce 8^2 particles each. The procedure is repeated recursively. In phase space (*bottom panel*) small points in the left-hand bottom corner represent the harmonics used for the low-resolution simulation. For the high-resolution run with box ratios 1:1/8:1/16 the phase space is sampled more coarsely, but high frequencies are included. Each harmonic (different markers) represents a small cube of the phase space indicated by squares. In this case the matching of the harmonics is not perfect: there are overlapping blocks and gaps. In any case, the waves inside domains A and B are missed in the simulation.

then 1024^3 particles. We simply do not have enough computer memory to store the information for all the harmonics. In this case we must decrease the resolution in the phase space. It is a bit easier to understand the procedure, if we consider phase-space diagrams like the one presented in figure 15.3. The low-resolution run in this case was done for 32^3 particles with harmonics up to $16 \times 2\pi/L$ (small points). For the high-resolution run we choose a region of size $1/8$ of the original large box. Inside the small box we place another box, which is twice as small. Thus, we will have three levels of mass refinement. For each level we have the corresponding size of the phase-space block. The size is defined by the size of real-space box and is equal to $2\pi/L \times K$, $K = 1, 8, 16$. Harmonics from different refinements should not overlap: if a region in the phase space is represented on a lower level of resolution, it should not appear in the higher resolution level. This is why the rows of the highest resolution harmonics (circles) with $K_x = 16$ and $K_y = 16$ are absent in figure 15.3: they have already been covered by the lower resolution blocks marked by stars. Figure 15.3 clearly illustrates that matching harmonics is a complicated process: we failed to do the match because there are partially overlapping blocks and there are gaps. We can get much better results, if we assume different ratios of the sizes of the boxes. For example, if instead of box ratios $1:1/8:1/16$, we choose ratios $1:3/32:5/96$, the coverage of the phase space is almost perfect as shown in figure 15.2.

15.2.4 Codes

There are many different numerical techniques to follow the evolution of a system of many particles. For earlier reviews see Hockney and Eastwood (1981), Sellwood (1987) and Bertschinger (1998). Most of the methods for cosmological applications take some ideas from three techniques: the Particle–Mesh (PM) code, direct summation or the Particle–Particle code and the TREE code. For example, the Adaptive Particle–Particle/Particle–Mesh (AP³M) code (Couchman 1991) is a combination of the PM code and the Particle–Particle code. The Adaptive-Refinement-Tree code (ART) (Kravtsov *et al* 1997, Kravtsov 1999) is an extension of the PM code with the organization of meshes in the form of a tree. All methods have their advantages and disadvantages.

15.2.4.1 The PM code

This uses a mesh to produce the density and potential. As a result, its resolution is limited by the size of the mesh. There are two advantages of the method: (i) it is fast (the smallest number of operations per particle per time step of all the other methods); and (ii) it typically uses a very large number of particles. The latter can be crucial for some applications. There are several modifications of the code. ‘Plain-vanilla’ PM was described by Hockney and Eastwood (1981). It includes a cloud-in-cell density assignment and a seven-point discrete analogue of the Laplacian operator. Higher-order approximations improve the accuracy on

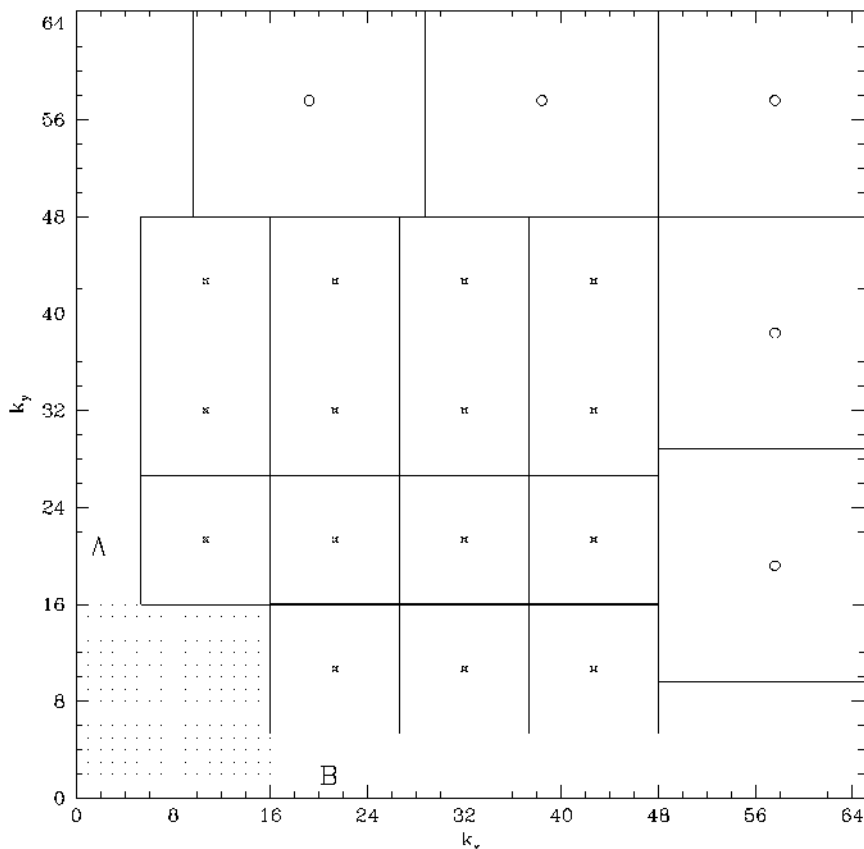


Figure 15.2. Another example of construction of mass refinement in phase space. For the high-resolution run with box ratios 1:3/3:5/96 the phase space is sampled without overlapping blocks or gaps.

large distances but degrades the resolution (e.g. Gelb 1992). The PM code is available (Klypin and Holtzman 1997).

15.2.4.2 The P^3M code

The P^3M code is described in detail in Hockney and Eastwood (1981) and Efsthathiou *et al* (1985). It has two parts: the PM part, which takes care of the large-scale forces; and the PP part, which adds the small-scale particle–particle contribution. Because of strong clustering at late stages in the evolution, the PP part becomes prohibitively expensive once large objects start to form in large numbers. A significant speed is achieved in a modified version of the code, which introduces sub-grids (the next levels of PM) in areas with high density

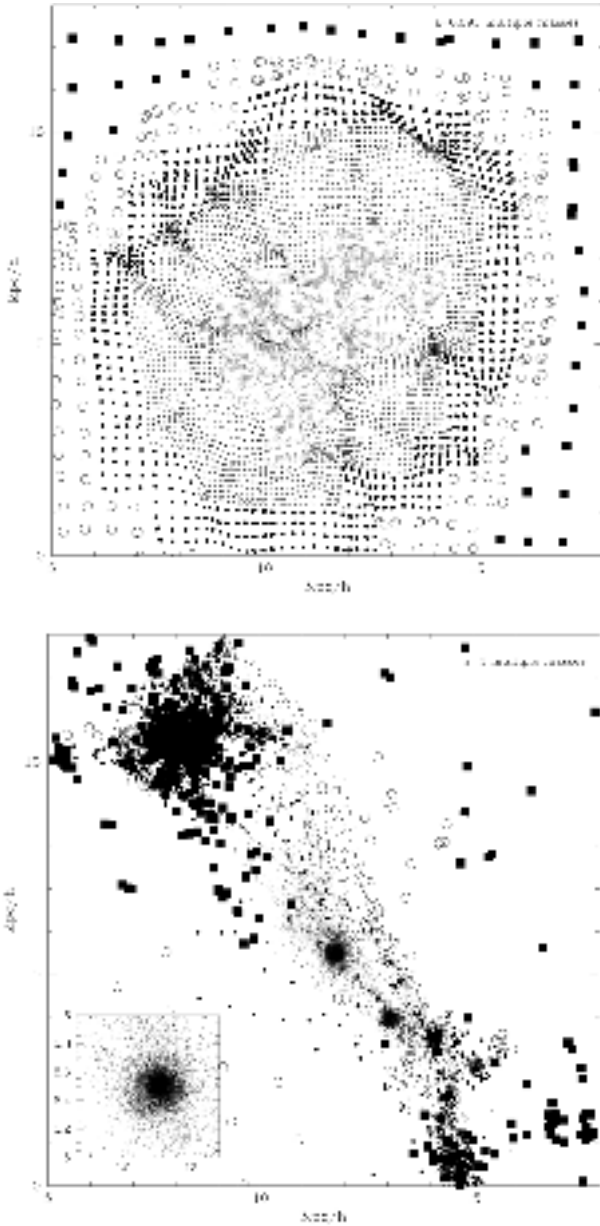


Figure 15.3. Distribution of particles of different masses in a thin slice going through the centre of halo A_1 at redshift 10 (top panel) and at redshift zero (bottom panel). To avoid crowding of points the thickness of the slice is made smaller in the centre (about $30h^{-1}$ kpc) and larger ($1h^{-1}$ Mpc) in the outer parts of the forming halo. Particles of different mass are shown with different symbols.

(Couchman 1991). With modification the code is as fast as the TREE code even for heavily clustered configurations. The code expresses the inter-particle force as a sum of a short-range force (computed by a direct particle–particle pair force summation) and the smoothly varying part (approximated by the particle–mesh force calculation). One of the major problems for these codes is the correct splitting of the force into a short-range and a long-range part. The grid method (PM) is only able to produce reliable inter-particle forces down to a minimum of at least two grid cells. For smaller separations the force can no longer be represented on the grid and therefore one must introduce a cut-off radius r_e (larger than two grid cells), where for $r < r_e$ the force should smoothly go to zero. The parameter r_e defines the chaining-mesh and for distances smaller than this cut-off radius r_e a contribution from the direct particle–particle (PP) summation needs to be added to the total force acting on each particle. Again this PP force should smoothly go to zero for very small distances in order to avoid unphysical particle–particle scattering. This cut-off of the PP force determines the overall force resolution of a P³M code.

The most widely used version of this algorithm is currently the adaptive P³M (AP³M) code of Couchman (1991), which is available publicly. The smoothing of the force in this code is connected to an S_2 sphere, as described in Hockney and Eastwood (1981).

15.2.4.3 *The TREE code*

The TREE code is the most flexible code in the sense of the choice of boundary conditions (Appel 1985, Barnes and Hut 1986, Hernquist 1987). It is also more expensive than PM: it takes 10–50 times more operations. Bouchet and Hernquist (1988) and Hernquist *et al* (1991) extended the code for periodical boundary conditions, which is important for simulating large-scale fluctuations. Some variants of TREE are publicly available. A very useful example is the GADGET code available at <http://www.mpa-garching.mpg.de/gadget/right.html>. There are variants of the code modified for massively parallel computers and there are variants with variable time stepping, which is vital for extremely high-resolution simulations.

15.2.4.4 *The ART code*

Multi-grid methods were introduced long ago, but only recently have they started to produce important results. Examples of adaptive multi-grid codes are the Adaptive Refinement Tree code (ART; Kravtsov *et al* 1997), the AMR code written by Bryan and Norman and MLAPM (Knebe *et al* 2001). The ART code reaches high-force resolution by refining all high-density regions with an automated refinement algorithm. The refinements are recursive: the refined regions can also be refined, each subsequent refinement having half of the previous level's cell size. This creates a hierarchy of refinement meshes with

different resolutions covering the regions of interest. The refinement is done cell-by-cell (individual cells can be refined or de-refined) and meshes are not constrained to have a rectangular (or any other) shape. This allows the code to refine the required regions in an efficient manner. The criterion for refinement is the *local overdensity* of particles: the code refines an individual cell only if the density of particles (smoothed with the cloud-in-cell scheme; Hockney and Eastwood 1981) is higher than n_{TH} particles, with typical values $n_{\text{TH}} = 2\text{--}5$. The Poisson equation on the hierarchy of meshes is solved first on the base grid using FFT techniques and then on the subsequent refinement levels. On each refinement level the code obtains the potential by solving the Dirichlet boundary problem with boundary conditions provided by the already existing solution at the previous level or from the previous moment of time.

Figure 15.4 (courtesy of A Kravtsov) gives an example of mesh refinement for the hydro-dynamical version of the ART code. The code produced this refinement mesh for a spherical strong explosion (Sedov solution).

The refinement of the time integration mimics the spatial refinement and the time step for each subsequent refinement level is twice as small as the step on the previous level. Note, however, that particles on the same refinement level move with the same step. When a particle moves from one level to another, the time step changes and its position and velocity are interpolated to appropriate time moments. This interpolation is first-order accurate in time, whereas the rest of the integration is done with the second-order accurate-time centred leap-frog scheme. All equations are integrated with the expansion factor a as a time variable and the global time step hierarchy is thus set by the step Δa_0 at the zeroth level (uniform base grid). The step on level L is then $\Delta a_L = \Delta a_0/2^L$.

What code is the best? Which one to choose? There is no unique answer—everything depends on the problem, which we are addressing. If you intend to study the structure of individual galaxies in the large-scale environment, you must have a code with very high resolution, variable time stepping and multiple masses. In this case the TREE or ART codes should be the choice.

15.2.5 Effects of resolution

As the resolution of the simulations improves and the range of their applications broaden, it becomes increasingly important to understand their limits. The effects of resolution and convergence studies were studied in a number of publications (e.g. Moore *et al* 1998, Frenk *et al* 1999, Knebe *et al* 2000, Ghigna *et al* 2000, Klypin *et al* 2001). Knebe *et al* (2000) made a detailed comparison of realistic simulations done with three codes: ART, AP³M and PM. Here we present some of their results and main conclusions. The simulations were done for the standard CDM model with the dimensionless Hubble constant $h = 0.5$ and $\Omega_0 = 1$. The simulation box of $15h^{-1}$ Mpc had 64^3 equal-mass particles, which gives the mass resolution (mass per particle) of $3.55 \times 10^9 h^{-1} M_\odot$. Because of the low resolution of the PM runs, we show results only for the other two codes. For the ART code

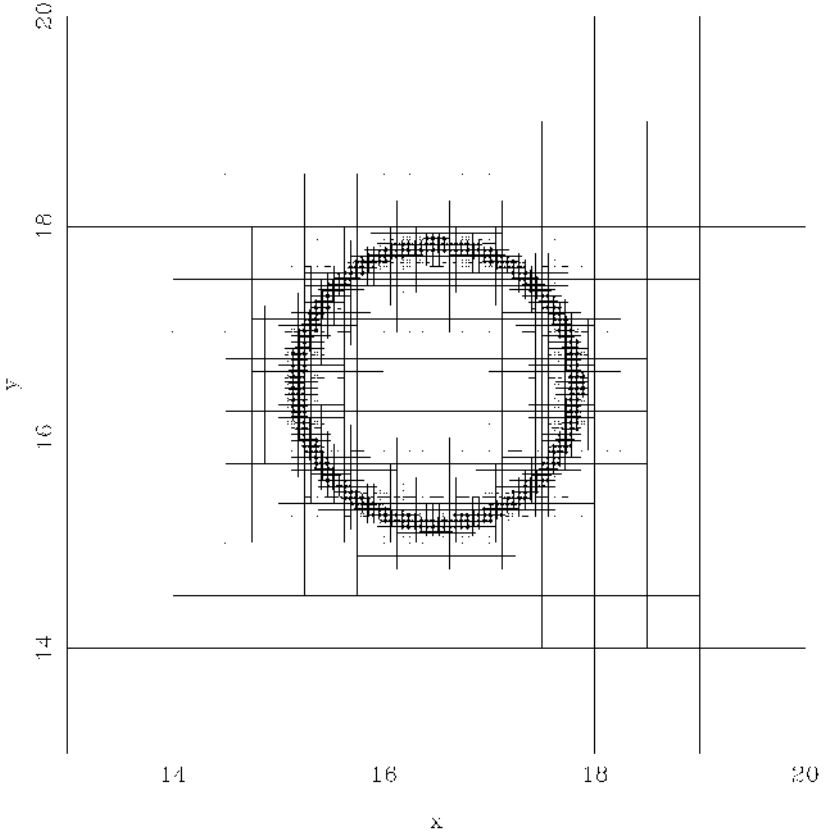


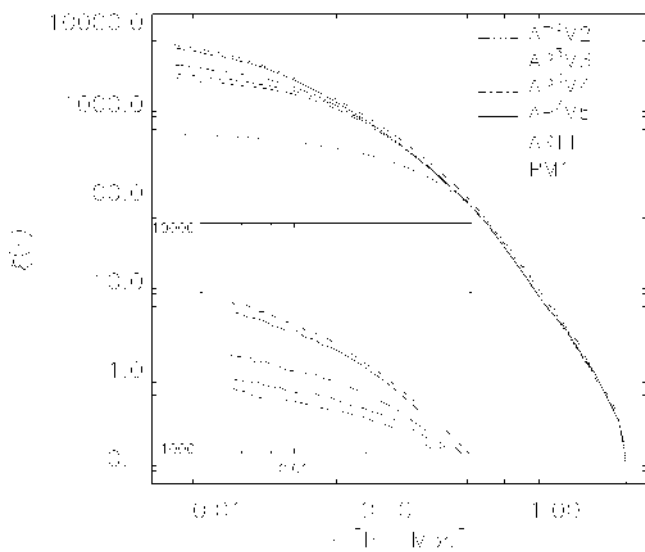
Figure 15.4. An example of a refinement structure constructed by the (hydro)ART code for spherical strong explosion (courtesy of A Kravtsov).

the force resolution is practically fixed by the number of particles. The only free parameter is the number of steps on the lowest (zero) level of resolution. In the case of the AP³M, besides the number of steps, one can also request the force resolution. Parameters from two runs with the ART code and five simulations with the AP³M are given in table 15.2.

Figure 15.5 shows the correlation function for the dark matter down to the scale of $5h^{-1}$ kpc, which is close to the force resolution of all our high-resolution simulations. The correlation function in the AP³M₁ and ART₂ runs are similar to those of AP³M₅ and ART₁ respectively and are not shown for clarity. We can see that the AP³M₅ and the ART₁ runs agree to $\lesssim 10\%$ over the whole range of scales. The correlation amplitudes of runs AP³M_{2–4}, however, are systematically lower at $r \lesssim 50\text{--}60h^{-1}$ kpc (i.e. the scale corresponding to $\approx 15\text{--}20$ resolutions), with the AP³M₃ run exhibiting the lowest amplitude. The fact that the AP³M₂

Table 15.2. Parameters of the numerical simulations.

Simulation	Softening (h^{-1} kpc)	Dyn. range	Steps (min–max)	$N_{\text{steps}}/\text{dyn. range}$
AP ³ M ₁	3.5	4267	8000	1.87
AP ³ M ₂	2.3	6400	6000	0.94
AP ³ M ₃	1.8	8544	6000	0.70
AP ³ M ₄	3.5	4267	2000	0.47
AP ³ M ₅	7.0	2133	8000	3.75
ART ₁	3.7	4096	660–21 120	2.58
ART ₂	3.7	4096	330–10 560	5.16

**Figure 15.5.** The correlation function of dark matter particles. Note that the range of correlation amplitudes is different in the inset panel.

correlation amplitude deviates less than that of the AP³M₃ run indicates that the effect is very sensitive to the force resolution.

Note that the AP³M₃ run has formally the best force resolution. Thus, one would naively expect that it would give the largest correlation function. At scales $\lesssim 30h^{-1}$ kpc the deviations of the AP³M₃ from the ART₁ or the AP³M₅ runs are ≈ 100 – 200% . We attribute these deviations to the numerical effects: the high force resolution in AP³M₃ was not adequately supported by the time integration. In other words, the AP³M₃ had too few time steps. Note that it had quite a large

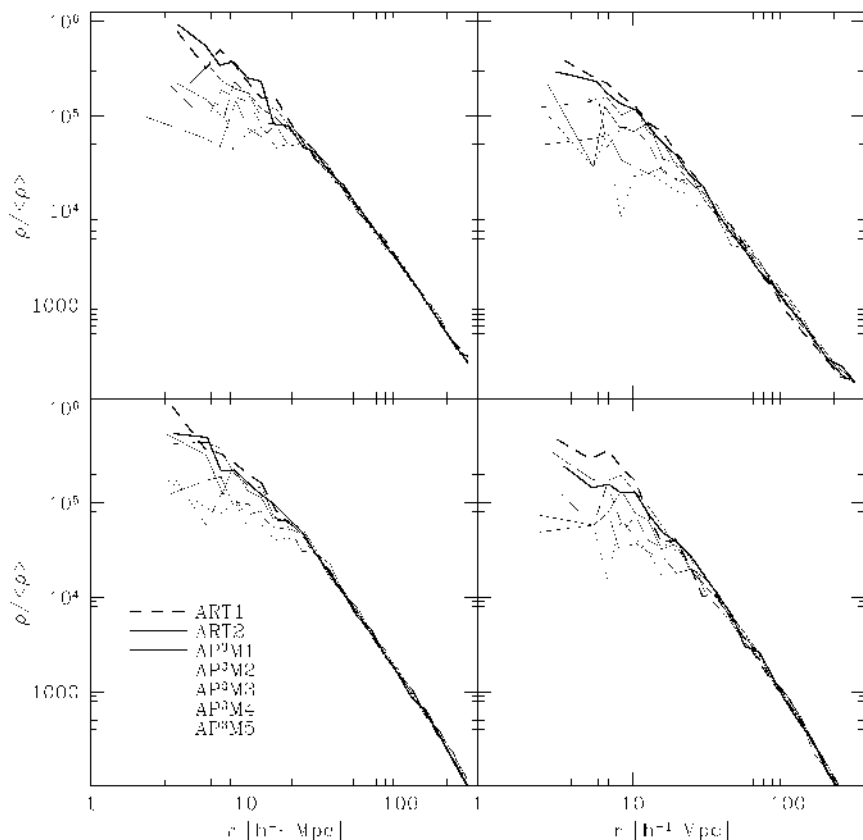


Figure 15.6. Density profiles of four largest halos in simulations of Knebe *et al* (1999). Note that the AP³M₃ run has formally the best force resolution, but its actual resolution was much lower because of an insufficient number of steps.

number of steps (6000), not much smaller than the AP³M₅ (8000). But for its force resolution, it should have many more steps. The lack of the number of steps was devastating.

Figure 15.6 presents the density profiles of four of the most massive halos in our simulations. We have not shown the profile of the most massive halo because it appears to have undergone a recent major merger and is not very relaxed. In this figure, we present only profiles of halos in the high-resolution runs. Not surprisingly, the inner density of the PM halos is much smaller than in the high-resolution runs and their profiles deviate strongly from the profiles of high-resolution halos at the scales shown in figure 15.6. A glance at figure 15.6 shows that all profiles agree well at $r \gtrsim 30h^{-1}$ kpc. This scale is about eight times smaller than the mean inter-particle separation. Thus, despite the very different

resolutions, time steps and numerical techniques used for the simulations, the convergence is observed at a scale much lower than the mean inter-particle separation, argued by Splinter *et al* (1998) to be the smallest trustworthy scale.

Nevertheless, there are systematic differences between the runs. The profiles in two ART runs are identical within the errors indicating convergence (we have run an additional simulation with time steps twice as small as those in the ART₁ finding no difference in the density profiles). Among the AP³M runs, the profiles of the AP³M₁ and AP³M₅ are closer to the density profiles of the ART halos than the rest. The AP³M₂, AP³M₃ and AP³M₄, despite the higher force resolution, exhibit lower densities in the halo cores, the AP³M₃ and AP³M₄ runs being the most deviant.

These results can be interpreted, if we examine the trend of the central density, as a function of the ratio of the number of time steps to the dynamic range of the simulations (see table 15.2). The ratio is smaller when either the number of steps is smaller or the force resolution is higher. The agreement in the density profiles is observed when this ratio is $\gtrsim 2$. This suggests that for a fixed number of time steps, there should be a limit on the force resolution. Conversely, for a given force resolution, there is a lower limit on the required number of time steps. The exact requirements would probably depend on the code type and the integration scheme. For the AP³M code our results suggest that the ratio of the number of time steps to the dynamic range should be no less than one. It is interesting that the deviations in the density profiles are similar to and are observed at the same scales as the deviations in the DM correlation function (figure 15.5), suggesting that the correlation function is sensitive to the central density distribution of dark matter halos.

15.2.6 Halo identification

Finding halos in dense environments is a challenge. Some of the problems that any halo-finding algorithm faces are not numerical. They exist in the real universe. We select a few typical difficult situations.

- (1) *A large galaxy with a small satellite.* Examples: LMC and the Milky Way or the M51 system. Assuming that the satellite is bound, do we have to include the mass of the satellite in the mass of the large galaxy? If we do, then we count the mass of the satellite twice: once when we find the satellite and then when we find the large galaxy. This does not seem reasonable. If we do not include the satellite, then the mass of the large galaxy is underestimated. For example, the binding energy of a particle at the distance of the satellite will be wrong. The problem arises when we try to assign particles to different halos in an effort to find the masses of halos. This is very difficult to do for particles moving between halos. Even if a particle at some moment has negative energy relative to one of the halos, it is not guaranteed that it belongs to the halo. The gravitational potential changes with time, and the particle may end up falling onto another halo. This is not just a precaution. This

actually was found very often in real halos when we compared the contents of halos at different redshifts. Interacting halos exchange mass and lose mass. We try to avoid the situation: instead of assigning mass to halos, we find the maximum of the ‘rotational velocity’, $\sqrt{GM/R}$, which, observationally, is a more meaningful quantity.

- (2) *A satellite of a large galaxy.* The previous situation is now viewed from a different angle. How can we estimate the mass or the rotational velocity of the satellite? The formal virial radius of the satellite is large: the big galaxy is within the radius. The rotational velocity may rise all the way to the centre of the large galaxy. In order to find the outer radius of the satellite, we analyse the density profile. At small distances from the centre of the satellite the density steeply declines, but then it flattens out and may even increase. This means that we have reached the outer border of the satellite. We use the radius at which the density starts to flatten out as the first approximation for the radius of the halo. This approximation can be improved by removing unbound particles and checking the steepness of the density profile in the outer part.
- (3) *Tidal stripping.* Peripheral parts of galaxies, responsible for extended flat rotation curves outside of clusters, are very likely tidally stripped and lost when the galaxies fall into a cluster. The same happens with halos: a large fraction of the halo mass may be lost due to stripping in dense cluster environments. Thus, if an algorithm finds that 90% of the mass of a halo identified at an early epoch is lost, it does not mean that the halo was destroyed. This is not a numerical effect and is not due to ‘lack of physics’. This is a normal situation. What is left of the halo, given that it still has a large enough mass and radius, is a ‘galaxy’.

There are different methods of identifying collapsed objects (halos) in numerical simulations.

The *Friends-Of-Friends (FOF)* algorithm was used a lot and still has its adepts. If we imagine that each particle is surrounded by a sphere of radius $bd/2$, then every connected group of particles is identified as a halo. Here d is the mean distance between particles, and b is called the *linking parameter*, which typically is 0.2. The dependence of groups on b is extremely strong. The method stems from an old idea of using percolation theory to discriminate between cosmological models. Because of this, FOF is also called the percolation method, which is wrong because the percolation is about groups spanning the whole box, not collapsed and compact objects. FOF was criticized for failing to find separate groups in cases when those groups were obviously present (Gelb 1992). The problem originates from the tendency of FOF to ‘percolate’ through bridges connecting interacting galaxies or galaxies in high-density backgrounds.

DENMAX tried to overcome the problems of FOF by dealing with density maxima (Gelb 1992, Bertschinger and Gelb 1991). It finds the maxima of density and then tries to identify particles, which belong to each maximum (halo). The

procedure is quite complicated. First, the density field is constructed. Second, the density (with a negative sign) is treated as a potential in which particles start to move as in a viscous fluid. Eventually, particles sink to the bottom of the potentials (which are also maxima density). Third, only particles with negative energy (relative to their group) are retained. Just as in the case of FOF, we can easily imagine situations when (this time) DENMAX should fail; for example, two colliding galaxies in a cluster of galaxies. They should just pass each other because of large relative velocity. In the moment of collision DENMAX ceases to ‘see’ both galaxies because all particles have positive energies. This is probably a quite unlikely situation. The method is definitely one of the best at present. The only problem is that it seems to be too complicated for the present state of simulations. DENMAX has two siblings—SKID (Stadel *et al*) and BDM (Klypin and Holtzman 1997)—which are frequently used.

‘*Overdensity 200*’. There is no name for this method, but it is often used. Find the density maximum, place a sphere and find the radius, within which the sphere has the mean overdensity 200 (or 177 if you really want to follow the top-hat model of nonlinear collapse).

15.3 Spatial and velocity biases

15.3.1 Introduction

The distribution of galaxies is probably biased with respect to the dark matter. Therefore, galaxies can be used to probe the matter distribution only if we understand the bias. Although the problem of bias has been studied extensively in the past (e.g. Kaiser 1984, Davis *et al* 1985, Dekel and Silk 1986), new data on high redshift clustering and the anticipation of coming measurements have recently generated substantial theoretical progress in the field. The breakthrough in an analytical treatment of the bias was the paper by Mo and White (1996), who showed how bias can be predicted in the framework of the extended Press–Schechter approximation. A more elaborate analytical treatment has been developed by Catelan *et al* (1998a, b), Porciani *et al* (1998) and Sheth and Lemson (1999). The effects of nonlinearity and stochasticity were considered in Dekel and Lahav (1999) (see also Taruya and Suto 2000).

Valuable results are produced by ‘hybrid’ numerical methods in which low-resolution N -body simulations (typical resolution ~ 20 kpc) are combined with semi-analytical models of galaxy formation (e.g. Diaferio *et al* 1999, Benson *et al* 2000, Somerville *et al* 2001). Typically, the results of these studies are very close to those obtained with brute-force approach of high-resolution ($\lesssim 2$ kpc) N -body simulations (e.g. Colín *et al* 1999, Ghigna *et al* 1998). This agreement is quite remarkable because the methods are very different. It may indicate that the biases of galaxy-size objects are controlled by the random nature of the clustering and merging of galaxies and by dynamical effects, which cause the merging, because those are the only common effects in those two approaches.

Direct N -body simulations can be used for studies of the biases only if they have very high mass and force resolution. Because of numerous numerical effects, halos in low-resolution simulations do not survive in dense environments of clusters and groups (e.g. Moore *et al* 1996, Tormen *et al* 1998, Klypin *et al* 1999a). Estimates of the necessary resolution are given in Klypin *et al* (1999a). Indeed, recent simulations, which have sufficient resolution, have found hundreds of galaxy-size halos moving inside clusters (Ghigna *et al* 1998, Colín *et al* 1999, Moore *et al* 1999, Okamoto and Habe 1999).

It is very difficult to make accurate and trustworthy predictions of luminosities for galaxies, which should be hosted by dark matter halos. Instead of luminosities or virial masses we suggest using circular velocities V_c for both numerical and observational data. For a real galaxy its luminosity tightly correlates with the circular velocity. So, one has a good idea what the circular velocity of the galaxy is. Nevertheless, direct measurements of circular velocities of a large complete sample of galaxies are extremely important because it will provide a direct way of comparing theory and observations. This chapter is mostly based on results presented in Colín *et al* (1999, 2000) and Kravtsov and Klypin (1999).

15.3.2 Oh, bias, bias

There are numerous aspects and notions related with the bias. One should be really careful to understand what type of bias is used. Results can be dramatically different. We start by introducing the overdensity field. If $\bar{\rho}$ is the mean density of some component (e.g. the dark matter or halos), then for each point \mathbf{x} in space we have $\delta(\mathbf{x}) \equiv [\rho(\mathbf{x}) - \bar{\rho}]/\bar{\rho}$. The overdensity can be decomposed into the Fourier spectrum, for which we can find the power spectrum $P(k) = \langle |\delta_k|^2 \rangle$. We can then find the correlation function $\xi(r)$ and the rms fluctuation of $\delta(R)$ smoothed on a given scale R . We can construct the statistics for each component: dark matter, galaxies or halos with given properties. Each statistics gives its own definition of bias b :

$$P_h(k) = b_p^2 P_h(k), \quad \xi_h(r) = b_\xi^2 \xi_{dm}(r), \quad \delta_h(R) = b_\delta \delta_{dm}(R). \quad (15.15)$$

The three estimates of the bias b are related. In a special case, when the bias is linear, local, and scale independent all three forms of bias are all equal. In general case they are different and they are complicated nonlinear functions of scale, mass of the halos or galaxies and redshift. The dependence on the scale is not local in the sense that the bias in a given position in space may depend on environment (e.g. density and velocity dispersion) on a larger scale. Bias has memory: it depends on the local history of the fluctuations. There is another complication: bias very likely is not a deterministic function. One source of this stochasticity is that it is non-local. Dependence on the history of clustering may also introduce some random effect.

There are some processes which we know create and affect the bias. At high redshifts there is statistical bias: in a Gaussian correlated field, high-density regions are more clustered than the field itself (Kaiser 1984). Mo and White (1996) showed how the extended Press–Schechter formalism can be used to derive of the bias of the dark matter halos. In the limit of small perturbations on large scales the bias is (Catelan *et al* 1998b, Taruya and Suto 2000)

$$b(M, z, z_f) = 1 + \frac{v^2 - 1}{\delta_c(z, z_f)}. \quad (15.16)$$

Here $v = \delta_c(z, z_f)/\sigma(M, z)$ is the relative amplitude of a fluctuation on scale M in units of the rms fluctuation $\sigma(M, z)$ of the density field at redshift z . The parameter z_f is the redshift of halo formation. The critical threshold of the top-hat model is $\delta_c(z, z_f) = \delta_{c,0}D(z)/D(z_f)$, where D is the growth factor of perturbations and $\delta_{c,0} = 1.69$. At high redshifts, parameter v for galaxy-size fluctuations is very large and δ_c is small. As a result, galaxy-size halos are expected to be more clustered (strongly biased) compared to the dark matter. The bias is larger for more massive objects. As the fluctuations grow, newly formed galaxy-size halos do not have such high peaks as at large redshifts and the bias tends to decrease. It also loses its sensitivity.

At later stages another process starts to change the bias. In group and cluster progenitors the merging and destruction of halos reduces the number of halos. This does not happen in the field where the number of halos of given mass may only increase with time. As a result, the number of halos inside groups and cluster progenitors is reduced relative to the field. This produces (anti)bias: there is a relatively smaller number of halos compared with the dark matter. This merging bias does not depend on the mass of halos and it has a tendency to slow down once a group becomes a cluster with a large relative velocity of halos (Kravtsov and Klypin 1999).

Here is a list of different types of bias. We classify them into three groups: (1) measures of bias, (2) terms related with the description of biases and (3) physical processes, which produce or change the bias.

15.3.2.1 Measures of bias

- (i) Bias measured in a statistical sense (e.g. ratio of correlation functions $\xi_h(r) = b^2\xi_{dm}(r)$).
- (ii) Bias measured point-by-point (e.g. $\delta_h(\mathbf{x}) - \delta_{dm}(\mathbf{x})$ diagrams).

15.3.2.2 Description of biases

- (i) Local and non-local bias. For example, $b(R) = \sigma_h(R)/\sigma_m(R)$ is the local bias. If $b = b(R; \tilde{R})$, the bias is non-local, where \tilde{R} is some other scale or scales.

- (ii) Linear and nonlinear bias. If in $\xi_h(r) = b^2 \xi_{\text{dm}}(r)$ the bias b does not depend on ξ_{dm} , it is the linear bias.
- (iii) Scale-dependent and scale-independent bias. If b does not depend on the scale at which the bias is estimated, the bias is scale independent. Note that, in general, the bias can be nonlinear and scale independent, but this highly unlikely.
- (iv) Stochastic and deterministic.

15.3.2.3 Physical processes, which produce or change the bias

- (i) Statistical bias. This arises when a specific subset of points is selected from a Gaussian field.
- (ii) Merging bias. This is produced due to merging and destruction of halos.
- (iii) Physical bias. This includes any bias due to physical processes inside forming galaxies.

15.3.3 Spatial bias

Colín *et al* (1999) have simulated different cosmological models and, using the simulations, have studied halo biases. Most of the results presented here are for the currently favoured Λ CDM model with the following parameters: $\Omega_0 = 1 - \Omega_\Lambda = 0.3$, $h = 0.7$, $\Omega_b = 0.032$, $\sigma_8 = 1$. The model was simulated with 256^3 particles in a $60h^{-1}$ Mpc box. The formal mass and force resolutions are $m_1 = 1.1 \times 10^9 h^{-1} M_\odot$ and $2h^{-1}$ kpc. The Bound Density Maximum halo finder was used to identify halos with at least 30 bound particles. For each halo we find the maximum circular velocity $V_c = \sqrt{GM(< r)/r}$.

In figure 15.7 we compare the evolution of the correlation functions of the dark matter and halos. There are remarkable differences between the halos and the dark matter. The correlation functions of the dark matter always increases with time (but the rate is different on different scales) and it is never a power law. The correlation function of the halos at redshifts decreases and then starts to increase again. It is accurately described by a power law with slope $\gamma = (1.5-1.7)$. Figure 15.8 presents a comparison of the theoretical and observational data on correlation functions and power spectra. The dark matter clearly predicts much too high a clustering amplitude. The halos are much closer to the observational points and predict antibias. For the correlation function the antibias appears on scales $r < 5h^{-1}$ Mpc; for the power spectrum the scales are $k > 0.2h$ Mpc $^{-1}$. One may get an impression that the antibias starts at longer waves in the power spectrum $\lambda = 2\pi/k \approx 30h^{-1}$ Mpc compared with $r \approx 5h^{-1}$ Mpc in the correlation function. There is no contradiction: sharp bias at small distances in the correlation function when Fourier transformed to the power spectrum produces antibias at very small wavenumbers. Thus, the bias should be taken into account at long waves when dealing with the power spectra. There is an inflection point in the power spectrum where the nonlinear power spectrum start to go upward (if

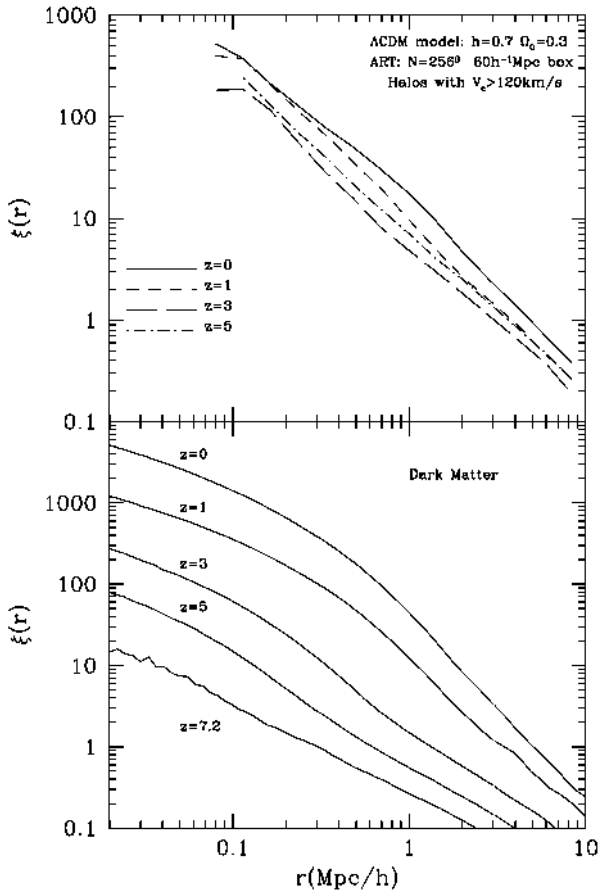


Figure 15.7. Evolution of the correlation function of the dark matter and halos. The correlation function of the dark matter increases monotonically with time. At any given moment it is not a power law. The correlation function of halos is a power law, but it is not monotonic in time.

one moves from low to high k) compared with the prediction of the linear theory. The exact position of this point may have been affected by the finite size of the simulation box $k_{\min} = 0.105h^{-1}$ Mpc, but the effect is expected to be small.

At $z = 0$ the bias hardly depends on the mass limit of the halos. There is a tendency of more massive halos to be more clustered at very small distances $r < 200h^{-1}$ kpc, but at this stage it is not clear that this is not due to residual numerical effects around centres of clusters. The situation is different at high redshift. At very high redshifts $z > 3$ galaxy-size halos are very strongly (positively) biased. For example, at $z = 5$ the correlation function of halos

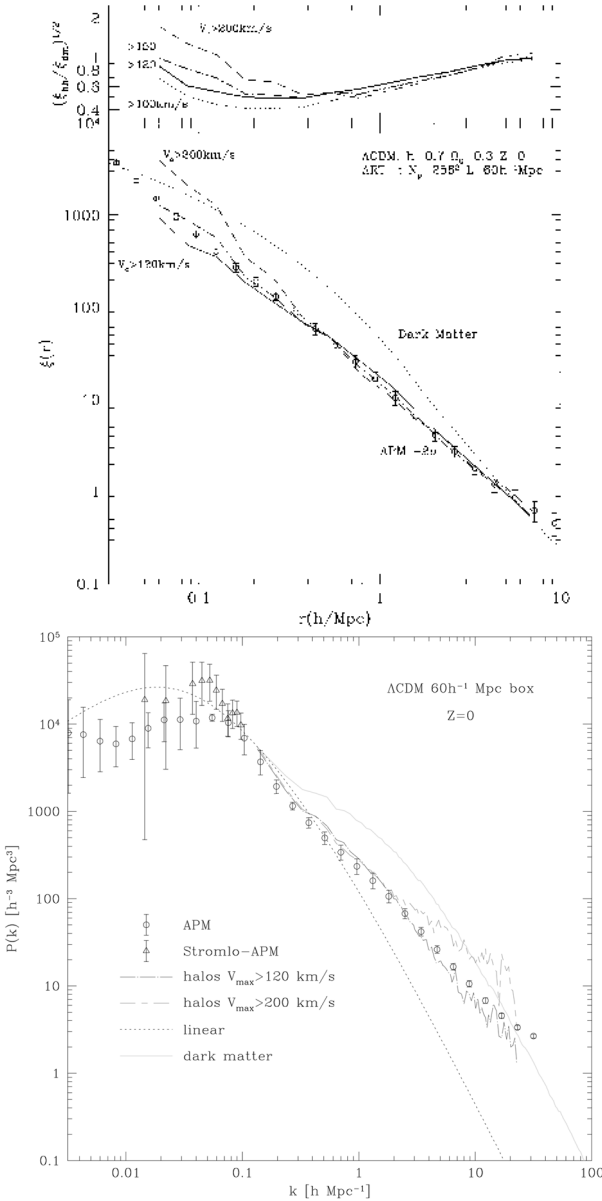


Figure 15.8. The correlation function and the power spectrum of halos with different limiting circular velocities in the Λ CDM model. The results are compared with the observational data from the APM and Stromlo-APM surveys. The bias is scale dependent but it does not depend much on the halo mass.

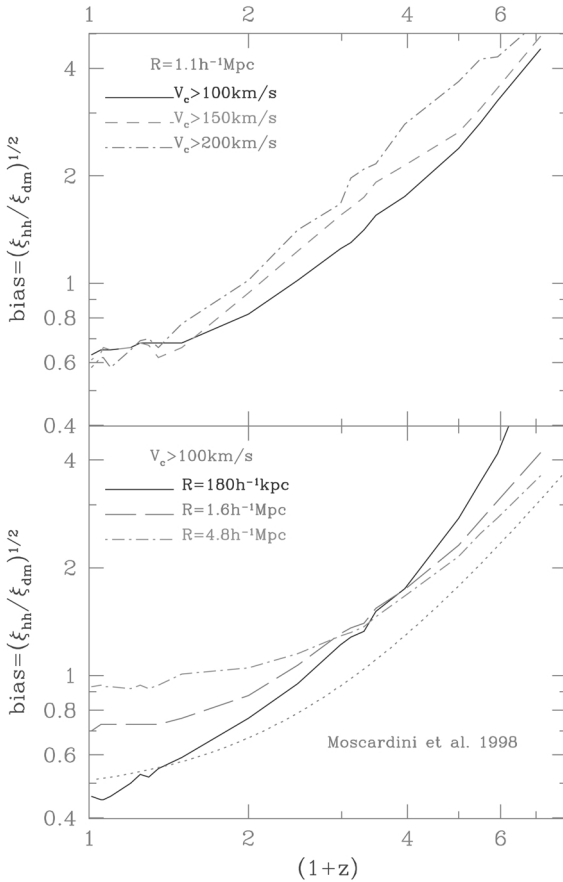


Figure 15.9. *Top panel:* The evolution of bias at comoving scale of $0.54 h^{-1} \text{Mpc}$ for halos with different circular velocities. *Bottom panel:* Dependence of the bias on the scale for halos with the same circular velocity.

with $v_c > 150 \text{ km s}^{-1}$ was 15 times larger than that of the dark matter at $r = 0.5 h^{-1} \text{Mpc}$ (see figure 8 in Colín *et al* (1999)). The bias was also very strongly mass-dependent with more massive halos being more clustered. At smaller redshifts the bias was declining quickly. Around $z = 1-2$ (the exact value depends on the halo circular velocity) the bias crossed unity and became less than unity (antibias) at later redshifts.

The evolution of bias is illustrated by figure 15.10. The figure shows that, at all epochs, the overdensity of halos tightly correlates with the overdensity of the dark matter. The slope of the relation depends on the dark matter density and evolves with time. At $z > 1$ halos are biased ($\delta_h > \delta_{\text{dm}}$) in overdense regions with

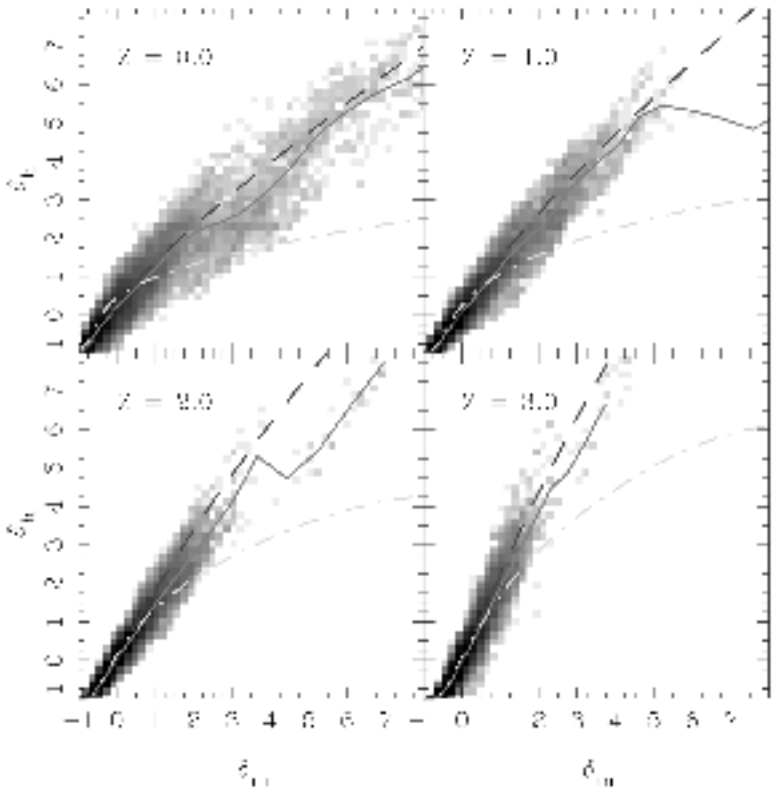


Figure 15.10. Overdensity of halos δ_h versus the overdensity of the dark matter δ_{dm} . The overdensities are estimated in spheres of radius $R_{TH} = 5h^{-1}$ Mpc. The intensity of the grey shade corresponds to the natural logarithm of the number of spheres in a two-dimensional grid in δ_h – δ_{dm} space. The full curves show the average relation. The chain curve is a prediction of an analytical model, which assumes that formation redshift z_f of halos coincides with observation redshift (typical assumption for the Press–Schechter approximation). The long-dashed curve is for a model, which assumes that the substructure survives for some time after it falls into a larger object: $z_f = z + 1$.

$\delta_{dm} > 1$ and antibiased in underdense regions with $\delta_{dm} < -0.5$. At low redshifts there is an antibias at large overdensities and almost no bias at low densities.

Figure 15.11 shows the density profiles for a cluster with mass $2.5 \times 10^{14}h^{-1}M_\odot$. There is antibias on scales below $300h^{-1}$ kpc. This is an example of the merging and destruction bias. Some of the halos have merged or were destroyed by the central cD halo of the cluster. As the result, there is a smaller number of halos in the central part compared with what we would expect if the number density of halos had followed the density of the dark matter (the full curve

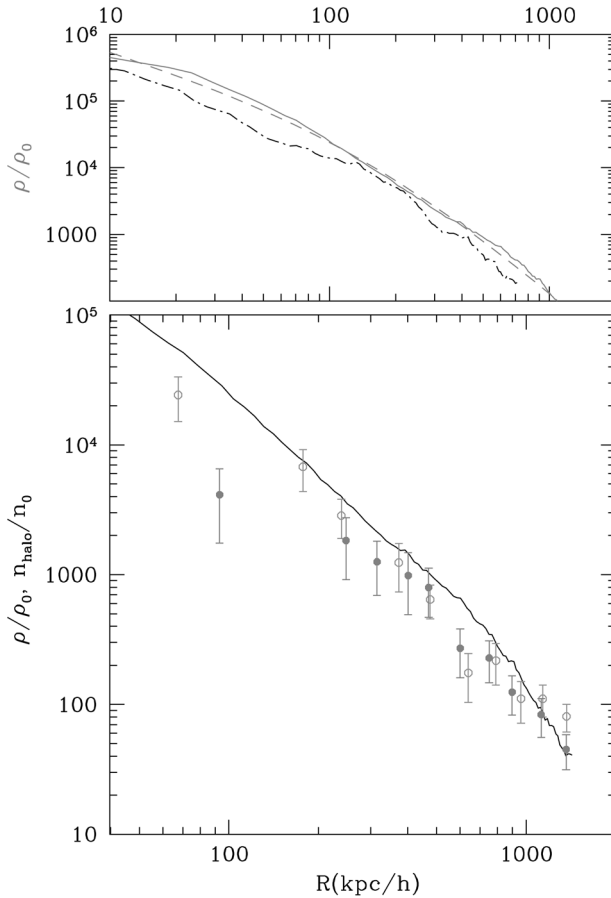


Figure 15.11. Density profiles for a cluster with mass $2.5 \times 10^{14} h^{-1} M_{\odot}$. *Top panel:* Dark matter density in units of the mean matter density at $z = 0$ (full curve) and at $z = 1$ (chain curve). The Navarro–Frenk–White profile (broken curve) provides a very good fit at $z = 0$. The $z = 1$ profile is given in proper (not comoving) units. *Bottom panel:* Number density profiles of halos in the cluster at $z = 0$ (full circles) and at $z = 1$ (open circles) compared with the $z = 0$ dark matter profile (full curve). There is antibias on scales below $300 h^{-1}$ kpc.

in the bottom panel). Note that, in the outer parts of the cluster, the halos closely follow the dark matter.

15.3.4 Velocity bias

There are two statistics, which measure velocity biases—differences in velocities of the galaxies (halos) and the dark matter. For a review of the results and

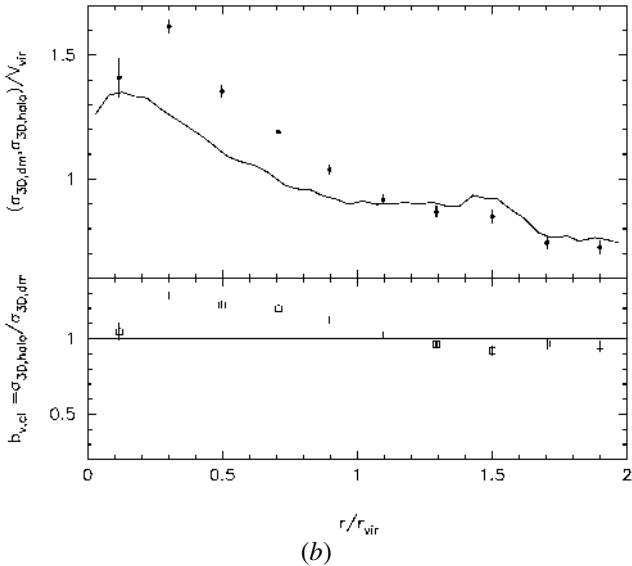
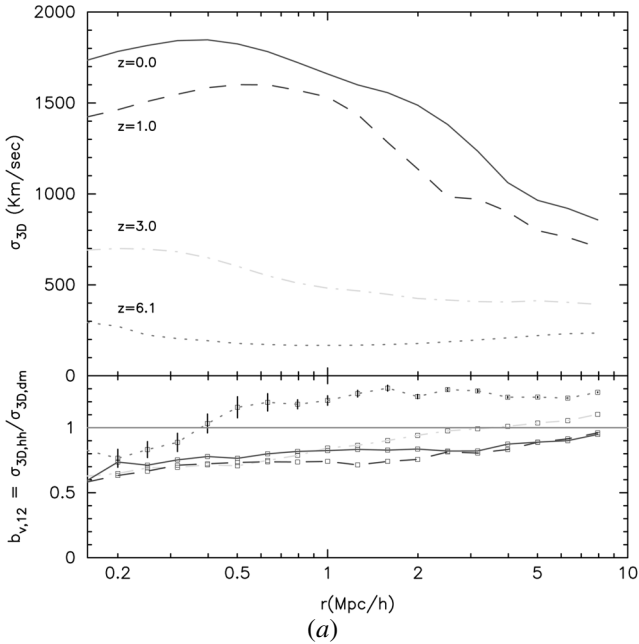


Figure 15.12. (a) Two-point velocity bias. (b) *Top panel:* 3D rms velocity for halos (circles) and for dark matter (full curve) in the 12 largest clusters. *Bottom panel:* velocity bias in the clusters. The bias in the first point increases to 1.2 if the central cD halos are excluded from analysis. Errors correspond to 1-sigma errors of the mean obtained by averaging over 12 clusters at two moments of time. Fluctuations for individual clusters are larger.

references see Colín *et al* (2000). Two-particle or pairwise velocity bias (PVB) measures the relative velocity dispersion in pairs of objects with given separation r : $b_{12} = \sigma_{h-h}(r)/\sigma_{dm-dm}(r)$. Figure 15.12 (left-hand panel) shows this bias. It is very sensitive to the number of pairs inside clusters of galaxies, where relative velocities are largest. Removal of a few pairs can substantially change the value of the bias. This ‘removal’ happens when halos merge or are destroyed by central cluster halos.

The one-point velocity bias is estimated as a ratio of the rms velocity of halos to that of the dark matter: $b_1 = \sigma_h/\sigma_{dm}$. It is typically applied to clusters of galaxies where it is measured at different distances from the cluster centre. For an analysis of the velocity bias in clusters, Colín *et al* (2000) have selected the 12 most massive clusters in a simulation of the Λ CDM model. The most massive cluster had virial mass $6.5 \times 10^{14} h^{-1} M_\odot$ comparable to that of the Coma cluster. The cluster had 246 halos with circular velocities larger than 90 km s^{-1} . There were three Virgo-type clusters with virial masses in the range $(1.6\text{--}2.4) \times 10^{14} h^{-1} M_\odot$ and with approximately 100 halos in each cluster. Just like the spatial bias, the PVB is positive at large redshifts (except for the very small scales) and decreases with the redshift. At lower redshifts it does not evolve much and stays below unity (antibias) at scales below $5h^{-1} \text{ Mpc}$ on level $b_{12} \approx (0.6\text{--}0.8)$.

Figure 15.13 shows the one-point velocity bias in clusters at $z = 0$. Note that the sign of the bias is now different: the halos move slightly faster than the dark matter. The bias is stronger in the central parts ($b_1 = 1.2\text{--}1.3$) and goes to almost no bias ($b_1 \approx 1$) at the virial radius and above. Both the antibias in the pairwise velocities and positive one-point bias are produced by the same physical process—merging and destruction of halos in the central parts of groups and clusters. The difference is in the different weighting of halos in these two statistics. A smaller number of high-velocity pairs significantly changes the PVB, but it only slightly affects the one-point bias because it is normalized to the number of halos at a given distance from the cluster centre. At the same time, merging preferentially happens for halos, which move with a smaller velocity at a given distance from the cluster centre. Slower halos have shorter dynamical times and have smaller apocentres. Thus, they have a better chance to be destroyed and merge with the central cD halo. Because low-velocity halos are eaten up by the central cD, the velocity dispersion of those which survive is larger. Another way of addressing the issue of velocity bias is to use the Jeans equations. If we have a tracer population, which is in equilibrium in a potential produced by mass $M(< r)$, then

$$-r\sigma_r^2(r) \left[\frac{d \ln \sigma_r^2(r)}{d \ln r} + \frac{d \ln \rho(r)}{d \ln r} + 2\beta(r) \right] = GM(< r), \quad (15.17)$$

where ρ is the number density of the tracer, β is the velocity anisotropy, and σ_r is the rms radial velocity. The right-hand side of the equation is the same for

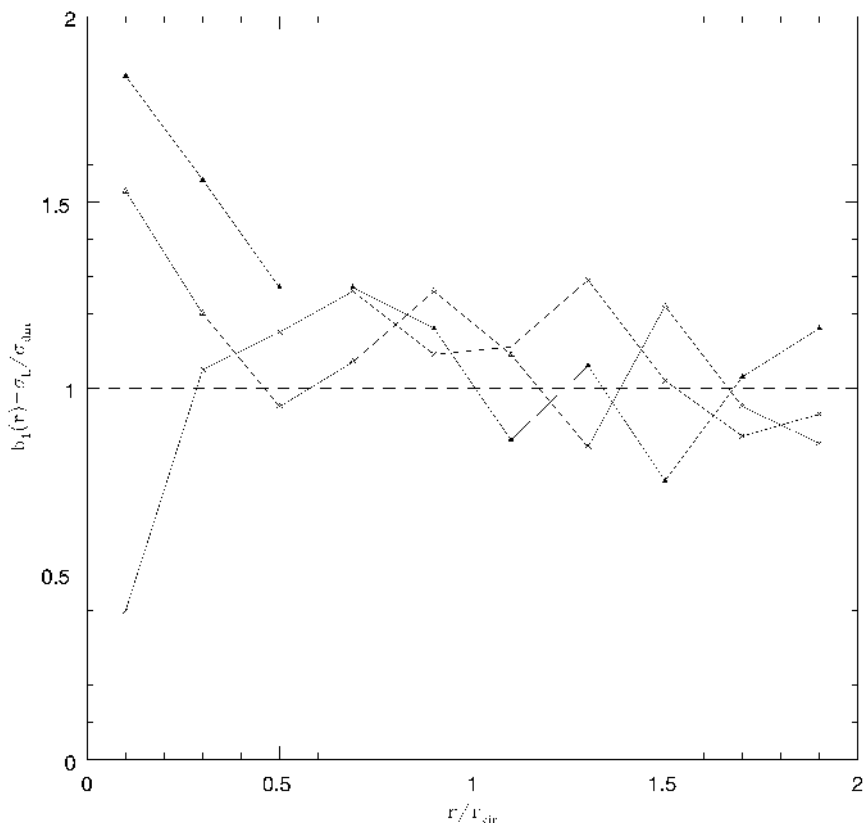


Figure 15.13. One-point velocity bias for three Virgo-type clusters in the simulation. Central cD halos are not included. Fluctuations in the bias are very large because each cluster has only ~ 100 halos with $V_c > 90 \text{ km s}^{-1}$ and because of substantial substructure in the clusters.

the dark matter and the halos. If the term in the brackets were to be the same, there would be no velocity bias. But there is systematic difference between the halos and the dark matter: the slope of the distribution halos in a cluster $\frac{d \ln \rho(r)}{d \ln r}$ is smaller than that of the dark matter (see Colín *et al* 1999, Ghigna *et al* 2000). The reason for the difference in the slopes is the same—merging with the central cD. Other terms in the equation also have small differences but the main contribution comes from the slope of the density. Thus, as long as we have spatial antibias of the halos, there should be a small positive one-point velocity bias in the clusters and a very strong antibias in the pairwise velocity. The exact values of the biases are still under debate, but one thing seems to be certain: the two biases go hand in hand.

The velocity bias in clusters is difficult to measure because it is small. Figure 15.12 may be misleading because it shows the average trend but it does not give the level of fluctuations for a single cluster. Note that the errors in the plots correspond to the error of the mean obtained by averaging over 12 clusters and two close moments of time. The fluctuations for a single cluster are much larger. Figure 15.12 shows results for three Virgo-type clusters in the simulation. The noise is very large both because of poor statistics (small number of halos) and the noise produced by residual non-equilibrium effects (substructure). A comparable (but slightly smaller) value of b_v was recently found in simulations by Ghigna *et al* (1999) for a cluster in the same mass range as that in figure 15.12. Unfortunately, it is difficult to make a detailed comparison with their results because Ghigna *et al* (1999) use only one hand-picked cluster for a different cosmological model. Very likely their results are dominated by the noise due to residual substructure. The results of another high-resolution simulation by Okamoto and Habe (1999) are consistent with our results.

15.3.5 Conclusions

There are a number of physical processes which can contribute to the biases. In this contribution we explore the dynamical effects in the dark matter itself, which result in differences in the spatial and velocity distribution of the halos and the dark matter. Other effects related to the formation of the luminous parts of galaxies can also produce or change biases. At this stage it is not clear how strong these biases are. Because there is a tight correlation between the luminosity and circular velocity of galaxies, any additional biases are limited by the fact that galaxies ‘know’ how much dark matter they have.

Biases in the halos are reasonably well understood and can be approximated on a few megaparsec scales by analytical models. We find that the biases in the distribution of the halos are sufficient to explain within the framework of standard cosmological models the clustering properties of galaxies on a vast ranges of scales from 100 kpc to dozens of megaparsecs. Thus, there is neither need nor much room for additional biases in the standard cosmological model.

In any case, biases in the halos should be treated as benchmarks for more complicated models, which include non-gravitational physics. If a model cannot reproduce the biases of halos or it does not have enough halos, it should be rejected, because it fails to give the correct dynamics for the main component of the universe—the dark matter.

15.4 Dark matter halos

15.4.1 Introduction

During the last decade there has been an increasing interest in testing the predictions of variants of the cold dark matter (CDM) models at sub-galactic

($\lesssim 100$ kpc) scales. This interest was first induced by indications that the observed rotation curves in the central regions of dark-matter-dominated dwarf galaxies are at odds with predictions of hierarchical models. Specifically, it was argued (Moore 1994, Flores and Primack 1994) that the circular velocities, $v_c(r) \equiv [GM(< r)/r]^{1/2}$, at small galactocentric radii predicted by the models are too high and increase too rapidly with increasing radius compared to the observed rotation curves. The steeper than expected rise in $v_c(r)$ implies that the *shape* of the predicted halo density distribution is incorrect and/or that the DM halos formed in CDM models are too concentrated (i.e. have too much of their mass concentrated in the inner regions).

In addition to the density profiles, there is an alarming mismatch in the predicted abundance of small-mass ($\lesssim 10^8 - 10^9 h^{-1} M_\odot$) galactic satellites and the observed number of satellites in the Local Group (Kauffmann *et al* 1993, Klypin *et al* 1999b, Moore *et al* 1999). Although this discrepancy may well be due to feedback processes such as photoionization that prevent gas collapse and star formation in the majority of the small-mass satellites (e.g. Bullock *et al* 2000), the mass scale at which the problem sets in is similar to the scale in the spectrum of primordial fluctuations that may be responsible for the problems with density profiles. In the age of precision cosmology that the forthcoming MAP and Planck cosmic microwave background anisotropy satellite missions are expected to bring about, tests of the cosmological models at small scales may prove to be the final frontier and the ultimate challenge to our understanding of the cosmology and structure formation in the universe. However, this obviously requires detailed predictions and checks from the theoretical side and higher resolution/quality observations and thorough understanding of their implications and associated caveats from the observational side. In this section we focus on the theoretical predictions of the density distribution of DM halos and some problems with comparing these predictions to observations.

A systematic study of halo density profiles for a wide range of halo masses and cosmologies was carried out by Navarro *et al* (1996, 1997; hereafter NFW), who argued that an analytical profile of the form $\rho(r) = \rho_s(r/r_s)^{-1}(1 + r/r_s)^{-2}$ provides a good description of halo profiles in their simulations for all halo masses and in all cosmologies. Here, r_s is the scale radius which, for this profile corresponds to the scale at which $d \log \rho(r)/d \log r|_{r=r_s} = -2$. The parameters of the profile are determined by the halo's virial mass M_{vir} and *concentration* defined as $c \equiv r_{\text{vir}}/r_s$. NFW argued that there is a tight correlation between c and M_{vir} , which implies that the density distributions of halos of different masses can, in fact, be described by a one-parameter family of analytical profiles. Further studies by Kravtsov *et al* (1997, 1999), Jing (2000) and Bullock *et al* (2001), although confirming the $c(M_{\text{vir}})$ correlation, indicated that there is a significant scatter in the density profiles and concentrations for DM halos of a given mass.

Following the initial studies by Moore (1994) and Flores and Primack (1994), Kravtsov *et al* (1999) presented a systematic comparison of the results of numerical simulations with rotation curves of a sample of 17 DM-dominated

dwarf and low-surface-brightness (LSB) galaxies. Based on these comparisons, we argued that there does not seem to be a significant discrepancy in the *shape* of the density profiles at the scales probed by the numerical simulations ($\gtrsim 0.02$ – $0.03r_{\text{vir}}$, where r_{vir} is the halo's virial radius). However, these conclusions were subject to several caveats and had to be tested. First, the observed galactic rotation curves had to be re-examined more carefully and with higher resolution. The fact that all of the observed rotation curves used in earlier analyses were obtained using relatively low-resolution HI observations, required checks of the possible beam smearing effects. Also, the possibility of non-circular random motions in the central regions that could modify the rotation velocity of the gas (e.g. Binney and Tremain 1987, p 198) had to be considered. Second, the theoretical predictions had to be tested for convergence and extended to scales $\lesssim 0.01r_{\text{vir}}$.

Moore *et al* (1998; see also a more recent convergence study by Ghigna *et al* 2000) presented a convergence study and argued that the mass resolution has a significant impact on the central density distribution of halos. They argued that at least several million particles per halo are required to model the density profiles at scales $\lesssim 0.01r_{\text{vir}}$ reliably. Based on these results, Moore *et al* (1999) advocated a density profile of the form $\rho(r) \propto (r/r_0)^{-1.5}[1 + (r/r_0)^{1.5}]^{-1}$, that behaves similarly ($\rho \propto r^{-3}$) to the NFW profile at large radii, but is steeper at small r : $\rho \propto r^{-1.5}$. Most recently, Jing and Suto (2000) presented a systematic study of density profiles for halo masses ranging from $2 \times 10^{12}h^{-1}M_{\odot}$ to $5 \times 10^{14}h^{-1}M_{\odot}$. The study was uniform in mass and force resolution featuring $\sim(5\text{--}10) \times 10^5$ particles per halo and a force resolution of $\sim 0.004r_{\text{vir}}$. They found that the galaxy-mass halos in their simulations are well fitted by profile[†] $\rho(r) \propto (r/r_0)^{-1.5}[1 + r/r_0]^{-1.5}$, but that cluster-mass halos are well described by the NFW profile, with a logarithmic slope of the density profiles at $r = 0.01r_{\text{vir}}$ changing from ≈ -1.5 for $M_{\text{vir}} \sim 10^{12}h^{-1}M_{\odot}$ to ≈ -1.1 for $M_{\text{vir}} \sim 5 \times 10^{14}h^{-1}M_{\odot}$. Jing and Suto interpreted these results as evidence that the profiles of DM halos are not universal.

The rotation curves of a number of dwarf and LSB galaxies have recently been reconsidered using H α observations (e.g. Swaters *et al* 2000, van den Bosch *et al* 2000). The results show that, for some galaxies, H α rotation curves are significantly different in their central regions than the rotation curves derived from HI observations. This indicates that the HI rotation curves are affected by beam smearing (Swaters *et al* 2000). It is also possible that some of the difference may be due to real differences in the kinematics of the two tracer gas components (ionized and neutral hydrogen). Preliminary comparisons of the new H α rotation curves with model predictions show that the NFW density profiles are consistent with the observed *shapes* of the rotation curves (van den Bosch *et al* 2000). Moreover, cusp density profiles with inner logarithmic slopes as steep as ~ -1.5 also seem to be consistent with the data (van den Bosch *et al* 2000). Nevertheless,

[†] Note that their profile is somewhat different from the profile advocated by Moore *et al*, but behaves similarly to the latter at small radii.

CDM halos appear to be too concentrated (Navarro and Swaters 2000, McGaugh *et al* 2000) compared to galactic halos and therefore the problem remains.

New observational and theoretical developments show that a comparison of model predictions to the data is not straightforward. Decisive comparisons require the convergence of theoretical predictions and understanding the kinematics of the gas in the central regions of the observed galaxies. In this section we present convergence tests designed to test the effects of mass resolution on the density profiles of halos formed in the currently popular CDM model with cosmological constant (Λ CDM) and simulated using the multiple mass resolution version of the Adaptive Refinement Tree code (ART). We also discuss some caveats in drawing conclusions about the density profiles from the fits of analytical functions to numerical results and their comparisons to the data.

15.4.2 Dark matter halos: the NFW and the Moore *et al* profiles

Before we fit the analytical profiles to real dark matter halos or compare them with observed rotational curves, it is instructive to compare different analytical approximations. Although the NFW and Moore *et al* profiles predict different behaviour for $\rho(r)$ in the central regions of a halo, the scale where this difference becomes significant depends on the specific values of the halo's characteristic density and radius. Table 15.3 presents the different parameters and statistics associated with the two analytical profiles. For the NFW profile more information can be found in Klypin *et al* (1999a, b, 2001), Lokas and Mamon (2000) and in Widrow (2000).

Each profile is set by two independent parameters. We choose these to be the characteristic density ρ_0 and radius r_s . In this case all expressions describing the different properties of the profiles have a simple form and do not depend on the concentration. The concentration or the virial mass appears only in the normalization of the expressions. The choice of the virial radius (e.g. Lokas and Mamon 2000) as a scale unit results in more complicated expressions with an explicit dependence on the concentration. In this case, one also has to be careful about the definition of the virial radius, as there are several different definitions in the literature. For example, it is often defined as the radius, r_{200} , within which the average density is 200 times the *critical density*. In this section the virial radius is defined as the radius within which the average density is equal to the density predicted by the top-hat model: it is δ_{TH} times the *average matter density* in the universe. For the $\Omega_0 = 1$ case the two existing definitions are equivalent. In the case of $\Omega_0 = 0.3$ models, however, the virial radius is about 30% larger than r_{200} .

There is no unique way of defining a consistent concentration for the different analytical profiles. Again, it is natural to use the characteristic radius r_s to define the concentration: $c \equiv r_{\text{vir}}/r_s$. This simplifies the expressions. At the same time, if we fit the same dark matter halo with the two profiles, we will get different concentrations because the values of the corresponding r_s will be different. Alternatively, if we choose to match the outer parts of the profiles

Table 15.3. Comparison of the NFW and Moore *et al* profiles.

Parameter	NFW	Moore <i>et al</i>
Density	$\rho = \frac{\rho_0}{x(1+x)^2}$	$\rho = \frac{\rho_0}{x^{1.5}(1+x)^{1.5}}$
$x = r/r_s$	$\rho \propto x^{-3}$ for $x \gg 1$	$\rho \propto x^{-3}$ for $x \gg 1$
	$\rho \propto x^{-1}$ for $x \ll 1$	$\rho \propto x^{-1.5}$ for $x \ll 1$
	$\rho/\rho_0 = 1/4.00$ at $x = 1$	$\rho/\rho_0 = 1/2.00$ at $x = 1$
	$\rho/\rho_0 = 1/21.3$ at $x = 2.15$	$\rho/\rho_0 = 1/3.35$ at $x = 1.25$
Mass		
$M = 4\pi\rho_0 r_s^3 f(x)$	$f(x) = \ln(1+x) - \frac{x}{1+x}$	$f(x) = \frac{2}{3} \ln(1+x^{3/2})$
$M = M_{\text{vir}} f(x)/f(C)$		
$M_{\text{vir}} = \frac{4}{3}\pi\rho_{\text{cr}}\Omega_0\delta_{\text{TH}}r_{\text{vir}}^3$		
Concentration	$C_{\text{NFW}} = 1.72C_{\text{Moore}}$	$C_{\text{Moore}} = C_{\text{NFW}}/1.72$
$C = r_{\text{vir}}/r_s$	(for the same M_{vir} and r_{max})	
	$C_{1/5} \approx \frac{C_{\text{NFW}}}{0.86f(C_{\text{NFW}})+0.1363}$	$C_{1/5} = \frac{C_{\text{Moore}}}{[(1+C_{\text{Moore}}^{3/2})^{1/5}-1]^{2/3}}$
(error <3% for $C_{\text{NFW}} = 5-30$)		$C_{0.0} \approx \frac{C_{\text{Moore}}}{[C_{\text{Moore}}^{3/10}-1]^{2/3}}$
	$C_{\gamma=-2} = C_{\text{NFW}}$	$C_{\gamma=-2} = 2^{3/2}C_{\text{Moore}}$
		$C_{\gamma=-2} \approx 2.83C_{\text{Moore}}$
Circular velocity		
$v_c^2 = \frac{GM_{\text{vir}}}{r_{\text{vir}}} \frac{C}{x} \frac{f(x)}{f(C)}$	$x_{\text{max}} \approx 2.15$	$x_{\text{max}} \approx 1.25$
$v_c^2 = v_{\text{max}}^2 \frac{x_{\text{max}}}{x} \frac{f(x)}{f(x_{\text{max}})}$	$v_{\text{max}}^2 \approx 0.216v_{\text{vir}}^2 \frac{C}{f(C)}$	$v_{\text{max}}^2 \approx 0.466v_{\text{vir}}^2 \frac{C}{f(C)}$
$v_{\text{vir}}^2 = \frac{GM_{\text{vir}}}{r_{\text{vir}}}$		

(say, $r > r_s$) as closely as possible, we may choose to change the ratio of the characteristic radii $r_{s,\text{NFW}}/r_{s,\text{Moore}}$ in such a way that both profiles reach the maximum circular velocity v_c at the same physical radius r_{max} . In this case, the formal concentration of the Moore *et al* profile is 1.72 times smaller than that of the NFW profile. Indeed, with this normalization the profiles look very similar in the outer parts as one finds in figure 15.14. Table 15.3 also gives two other ‘concentrations’. The concentration $C_{1/5}$ is defined as the ratio of virial radius to the radius, which encompasses one-fifth of the virial mass (Avila-Reese *et al* 1999). For halos with $C_{\text{NFW}} \approx 5.5$ this one-fifth mass concentration is equal to C_{NFW} . One can also define the concentration as the ratio of the virial radius to the radius at which the logarithmic slope of the density profile is equal to -2 . This scale corresponds to r_s for the NFW profile and $\approx 0.35r_s$ for the Moore *et al* profile.

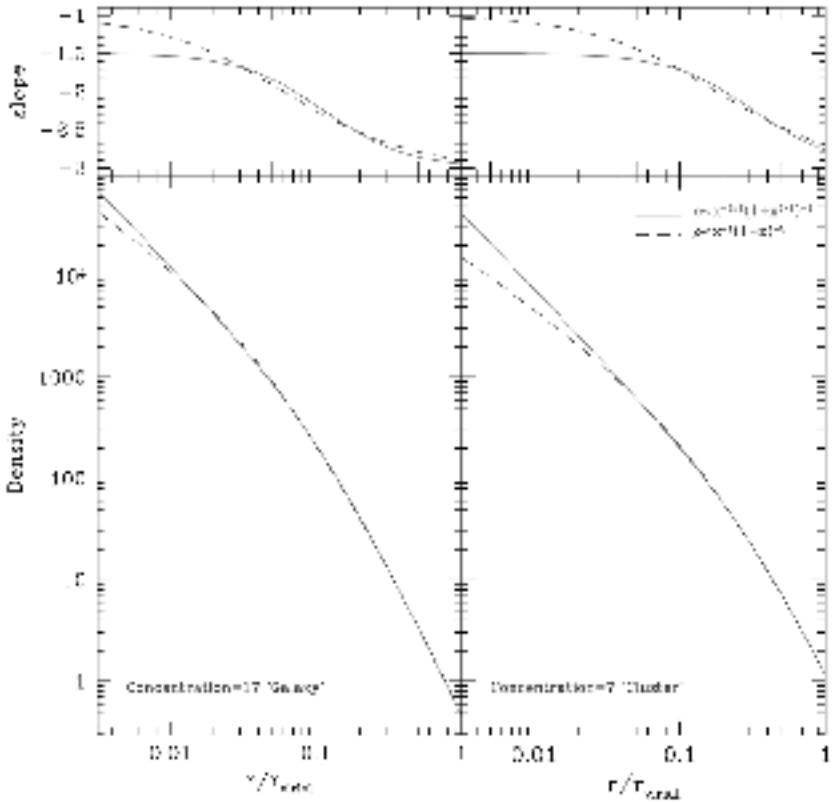


Figure 15.14. Comparison of the Moore *et al* and NFW profiles. Each profile is normalized to have the same virial mass and the same radius of the maximum circular velocity. *Left panels:* High-concentration halo with concentrations typical for small galaxies $C_{\text{NFW}} = 17$. *Right panels:* Low-concentration halo with concentrations typical for clusters of galaxies. The deviations are very small ($< 3\%$) for radii $r > 1/2 r_s$. The top panels show the local logarithmic slope of the profiles. Note that for the high concentration halo the slope of the profile is significantly larger than the asymptotic value -1 even at very small radii $r \approx 0.01/r_{\text{vir}}$.

Figure 15.14 presents a comparison of the analytic profiles normalized to have the same virial mass and the same radius r_{max} . We show the results for halos with low and high concentration values which are representative of cluster- and low-mass galaxy halos, respectively. The bottom panels show the profiles, while the top panels show the corresponding logarithmic slope as a function of the radius. The figure shows that the two profiles are very similar throughout the main body of the halos. Only in the very central region do the differences become significant. The difference is more apparent in the logarithmic slope than in the

actual density profiles. Moreover, for galaxy-mass halos the difference sets in at a rather small radius ($\lesssim 0.01 r_{\text{vir}}$), which would correspond to scales less than 1 kpc for the typical DM-dominated dwarf and LSB galaxies. In most analyses involving galaxy-size halos, the differences between the NFW and Moore *et al* profiles are irrelevant, and the NFW profile should provide an accurate description of the density distribution.

Note also that for galaxy-size (e.g. high-concentration) halos the logarithmic slope of the NFW profile does not reach its asymptotic inner value of -1 at scales as small as $0.01 r_{\text{vir}}$. For $\sim 10^{12} h^{-1} M_{\odot}$ halos the logarithmic slope of the NFW profile is ≈ -1.4 – 1.5 , while for cluster-size halos this slope is ≈ -1.2 . This dependence of slope at a given fraction of the virial radius on the virial mass of the halo is very similar to the results plotted in figure 3 of Jing and Suto (2000). They interpreted it as evidence that the halo profiles are not universal. It is obvious, however, that their results are consistent with the NFW profiles and the dependence of the slope on mass can simply be a manifestation of the well-studied $c_{\text{vir}}(M)$ relation.

To summarize, we find that the differences between the NFW and Moore *et al* profiles are very small ($\Delta\rho/\rho < 10\%$) for radii above 1% of the virial radius. The differences are larger for halos with smaller concentrations. For the NFW profile, the asymptotic value of the central slope $\gamma = -1$ is not achieved even at radii as small as 1–2% of the virial radius.

15.4.3 Properties of dark matter halos

Some properties of halos depend on the large-scale environment in which the halos are found. We will call a halo *distinct* if it is not inside a virial radius of another (larger) halo. A halo is called a *sub-halo* if it is inside another halo. The number of sub-halos depends on the mass resolution—the deeper we go, the more sub-halos we will find. Most of the results given here are based on a simulation, which was complete to masses down to $10^{11} h^{-1} M_{\odot}$ or, equivalently, to the maximum circular velocity of 100 km s^{-1} .

15.4.3.1 Mass and velocity distribution functions

The halo mass and velocity function has been extensively analysed by Sigad *et al* (2000) for halos in the Λ CDM model. Additional results can also be found in Ghigna *et al* (1999), Moore *et al* (1999), Klypin *et al* (1999b) and Gottlöber *et al* (1998). Figure 15.15 compares the mass function of sub-halos and distinct halos. The Press–Schechter approximation overestimates the mass function by a factor of two for $M < 5 \times 10^{12} h^{-1} M_{\odot}$ and it somewhat underestimates it at larger masses. A more advanced approximation given by Sheth and Tormen is more accurate. On scales below $10^{14} h^{-1} M_{\odot}$ the mass function is close to a power law with slope $\alpha \approx -1.8$. There is no visible difference in the slope for sub-halos and for the distinct halos.

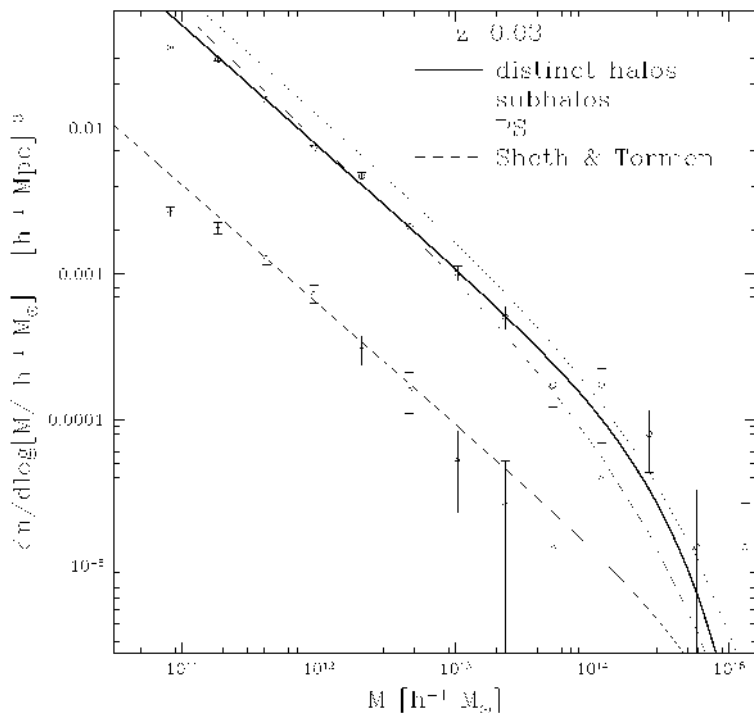


Figure 15.15. The mass function for distinct halos (top) and for sub-halos (bottom). Raw counts are marked by symbols with error bars. The curves are Schechter-function fits. The Press–Schechter (dotted) and Sheth–Tormen (dashes) predictions for distinct halos are also shown. On scales below $10^{14} h^{-1} M_{\odot}$ the mass function is close to a power law with slope $\alpha \approx -1.8$. There is no visible difference in the slope for sub-halos and that for distinct halos. (After Sigad *et al* 2000.)

For each halo one can measure the maximum circular velocity V_{\max} . In many cases (especially for sub-halos) V_{\max} is a better measure of the size of the halo. It is also related more closely with the observed properties of galaxies hosted by halos. Figure 15.16 presents the velocity distribution functions of different types of halo. In addition to distinct halos and sub-halos, we also show isolated halos and halos in groups and clusters. Here isolated halos are defined as halos with a mass less than $10^{13} h^{-1} M_{\odot}$, which are not inside a larger halo and which do not have sub-halos more massive than $10^{11} h^{-1} M_{\odot}$. The velocity function is approximated by a power law $dn = \Phi_* V_{\max}^{\beta} dV_{\max}$ with slope $\beta \approx -3.8$ for distinct halos. The slope depends on the environment: $\beta \approx -3.1$ for halos in groups and $\beta \approx -4$ for isolated halos. Klypin *et al* (1999b) and Ghigna *et al* (1999) found that the slope $\beta \approx -3.8$ – -4 of the velocity function extends to much smaller halos with velocities down to 10 km s^{-1} .

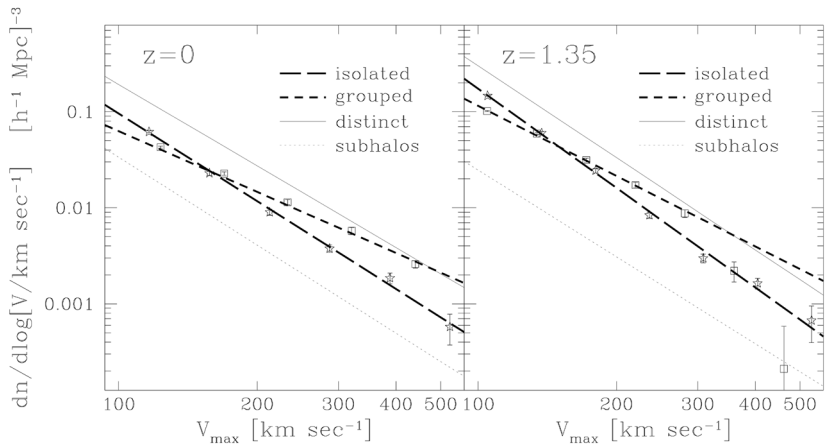


Figure 15.16. Velocity functions for isolated halos (squares) and for halos in groups and clusters. Halos with mass less than $10^{13} h^{-1} M_{\odot}$ are used for the plots. (After Sigad *et al* 2000.)

15.4.3.2 Correlation between characteristic density and radius

The halo density profiles are approximated by the NFW profile:

$$\rho = \frac{\rho_0}{(r/r_0)[1 + r/r_0]^2}. \quad (15.18)$$

Kravtsov *et al* (1999) found the correlation between the two parameters of halos: ρ_0 and r_s . Figure 15.17 compares the results for the DM halos with those for DM-dominated, LSB galaxies and dwarf galaxies. The halos are consistent with observational data: smaller halos are denser.

15.4.3.3 Correlations between mass, concentration and redshift

Navarro *et al* (1997) argued that the halo profiles have a universal shape in the sense that the profile is uniquely defined by the virial mass of the halo. Bullock *et al* (2001) analysed concentrations of thousands of halos at different redshifts. To some degree they confirm the conclusions of Navarro *et al* (1997): halo concentration correlates with its mass. However, some significant deviations were also found. There is no one-to-one relation between concentration and mass. It appears the the universal profile should only be treated as a trend: the halo concentration does increase as the halo mass decreases, but there are large deviations for individual halos from that ‘universal’ shape. Halos have an intrinsic scatter of concentration: at the 1σ level halos with the same mass have $\Delta(\log c_{\text{vir}}) = 0.18$ or, equivalently, $\Delta V_{\text{max}}/V_{\text{max}} = 0.12$.

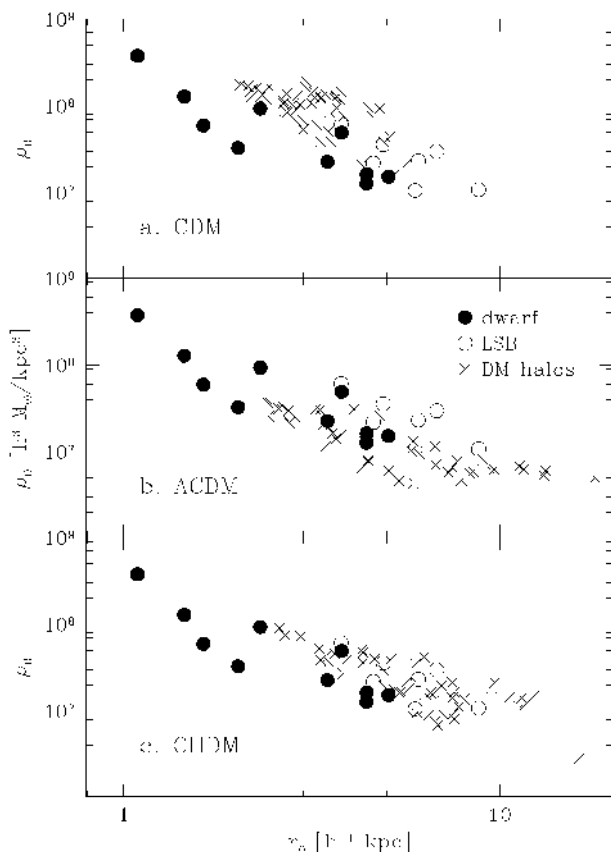
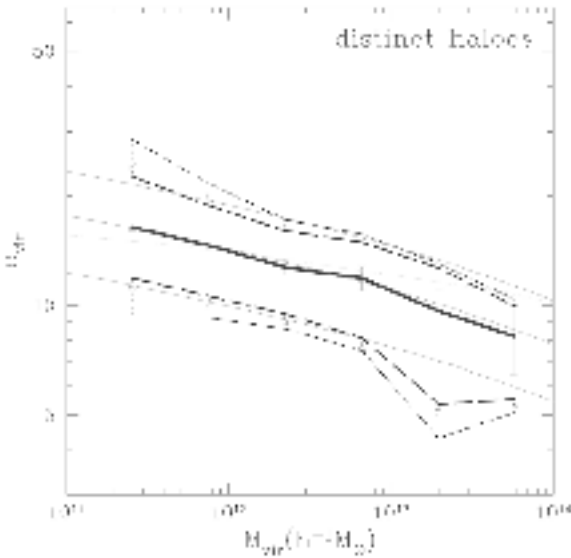


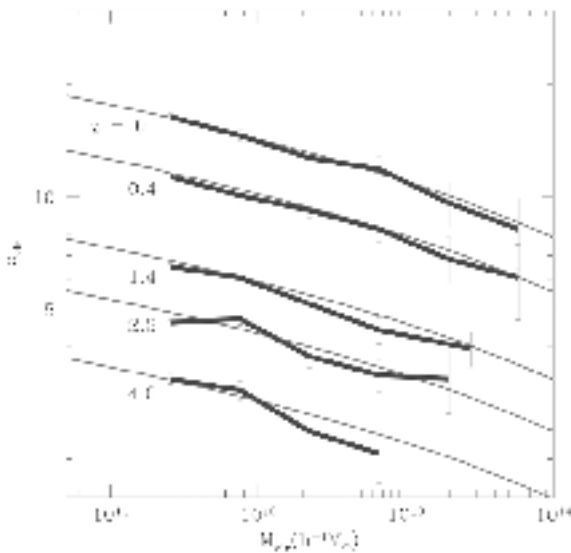
Figure 15.17. Correlation of the characteristic density ρ_0 and radius r_0 for the dwarf and LSB galaxies (full and open circles) and for DM halos (crosses) in different cosmological models. The halos are consistent with observational data: smaller halos are denser. (After Kravtsov *et al* 1999.)

15.4.3.4 Velocity anisotropy

Inside a large halo, sub-halos or DM particles do not move on either circular or radial orbits. A velocity ellipsoid can be measured at each position inside a halo. It can be characterized by an anisotropy parameter defined as $\beta(r) = 1 - V_{\perp}^2/2V_r^2$. Here V_{\perp}^2 is the velocity dispersion perpendicular to the radial direction and V_r^2 is the radial velocity dispersion. For pure radial motions $\beta = 1$. For isotropic velocities $\beta = 0$. The function $\beta(r)$ was estimated for halos in different cosmological models (see Colín *et al* 1999 for references). By studying 12 rich clusters with many sub-halos inside each of them, Colín *et al* (1999) found that both the sub-halos and DM particles can be described by the same anisotropy



(a)



(b)

Figure 15.18. (a) Dependence of concentration with mass for distinct halos. The bold full curve is the median value. The errors are errors of the mean due to sampling. The outer chain curves encompass 68% of halos in the simulations. The broken curves and arrows indicate values corrected for the noise in halo profiles. Thin curves are different analytical models. (b) Median halo concentration as a function of mass for different redshifts. The thin lines show the predictions of an analytical model. (After Bullock *et al* 2001.)

parameter

$$\beta(r) = 0.15 + \frac{2x}{x^2 + 4}, \quad x = r/r_{\text{vir}}. \quad (15.19)$$

15.4.4 Halo profiles: convergence study

The following results are based on Klypin *et al* (2001).

15.4.4.1 Numerical simulations

Using the ART code (Kravtsov *et al* 1997, Kravtsov 1999), we simulate a flat low-density cosmological model (Λ CDM) with $\Omega_0 = 1 - \Omega_\Lambda = 0.3$, the Hubble parameter (in units of $100 \text{ km s}^{-1} \text{ Mpc}^{-1}$) $h = 0.7$, and the spectrum normalization $\sigma_8 = 0.9$. We run two sets of simulations with $30h^{-1} \text{ Mpc}$ and $25h^{-1} \text{ Mpc}$ computational box. The first simulations were run to the present moment $z = 0$. The second set of simulations had higher mass resolution and therefore produced more halos but were run only to $z = 1$.

In all our simulations the step in the expansion parameter was chosen to be $\Delta a_0 = 2 \times 10^{-3}$ on the zero level of resolution. This gives about 500 steps for an entire run to $z = 0$. A test run was done with a time step twice as small as that for a halo of comparable mass (but with a smaller number of particles) as studied in this chapter. We did not find any visible deviations in the halo profile. In the first set of simulations, the highest refinement level was ten, which corresponds to $500 \times 2^{10} \approx 500\,000$ time steps at the tenth level. For the second set of simulations, nine levels of refinement were reached which corresponds to 128 000 steps at the ninth level.

In the following sections we present the results for four halos. The first halo (A) was the only halo selected for re-simulation in the first set of simulations. In this case the selected halo was relatively quiescent at $z = 0$ and had no massive neighbours. The halo was located in a long filament bordering a large void. It was about 10 Mpc away from the nearest cluster-size halo. After the high-resolution simulation was completed we found that the nearest galaxy-size halo was about 5 Mpc away. The halo had a fairly typical merging history with an $M(t)$ track slightly lower than the average mass growth predicted using extended Press–Schechter model. The last major merger event occurred at $z \approx 2.5$; at lower redshifts the mass growth (the mass in this time interval has grown by a factor of three) was due to slow and steady mass accretion.

The second set of simulations was done in a different way. In the low-resolution run we selected three halos in a well-pronounced filament. Two of the halos were neighbours located at about 0.5 Mpc from each other. The third halo was 2 Mpc away from this pair. Thus, the halos were not selected to be too isolated as was the case in the first set of runs. Moreover, the simulation was analysed at an earlier moment ($z = 1$) where halos are more likely to be unrelaxed. Therefore, we consider the halo A from the first set as an example

Table 15.4. Parameters of halos.

z	M_{vir}	R_{vir}	V_{max}	N_{part}	m_{part}	Form. res.	C_{NFW}	RelEr	RelEr	
	M_{\odot}/h	kpc h^{-1}	km s $^{-1}$		M_{\odot}/h	kpc h^{-1}		NFW	Moore	
(1)	(2)	(3)	(4)	(5)	(6)	(7)	(8)	(9)	(10)	(11)
A ₁	0	1.97×10^{12}	257	247.0	1.2×10^5	1.6×10^7	0.23	17.4	0.17	0.20
A ₂	0	2.05×10^{12}	261	248.5	1.5×10^4	1.3×10^8	0.91	16.0	0.13	0.16
A ₃	0	1.98×10^{12}	256	250.5	1.9×10^3	1.1×10^9	3.66	16.6	0.16	0.10
B	1	8.5×10^{11}	241	195.4	7.1×10^5	1.2×10^6	0.19	12.3	0.23	0.16
C	1	6.8×10^{11}	208	165.7	5.0×10^5	1.2×10^6	0.19	11.9	0.37	0.20
D	1	9.6×10^{11}	245	202.4	7.9×10^5	1.2×10^6	0.19	9.5	0.25	0.60

of a rather isolated well-relaxed halo. In many respects, this halo is similar to halos simulated by other research groups that used multiple mass resolution techniques. The three halos from the second set of simulations can be viewed as being representative of more typical halos, not necessarily well relaxed and located in more crowded environments.

The parameters of the simulated DM halos are listed in table 15.4. Columns represent:

- (1) the halo ‘name’ (halos A₁, A₂, A₃ are halo A re-simulated with different resolutions);
- (2) the redshift at which the halo was analysed;
- (3)–(5) the virial mass, comoving virial radius and maximum circular velocity.
At $z = 0$ ($z = 1$) the virial radius was estimated as the radius within which the average overdensity of matter is 340 (180) times larger than the mean cosmological density of matter at that redshift;
- (6) the number of particles within the virial radius;
- (7) the smallest particle mass in the simulation;
- (8) formal force resolution achieved in the simulation. As we will show later, convergent results are expected at scales larger than four times the formal resolution;
- (9) the halo concentration as estimated from NFW profile fits to halo density profiles;
- (10) the maximum relative error of the NFW fit: $\rho_{\text{NFW}}/\rho_{\text{h}} - 1$ (the error was estimated inside $50h^{-1}$ kpc radius);
- (11) the same as in the previous column, but for the fits of profile advocated by Moore *et al.*

Halo A in the first set of simulations was re-simulated three times with increasing mass resolution. For each simulation, we considered outputs at four moments in the interval to $z = 0$ –0.03. The parameters of the halos in these simulations averaged over the four moments are presented in the first three rows of table 15.4. We did not find any systematic change with resolution in the values

of the halo parameters either on the virial radius scale or around the maximum of the circular velocity ($r = (30\text{--}40)h^{-1}$ kpc).

The top panel in figure 15.19 shows the central region of halo A₁ (see table 15.4). This plot is similar to figure 1(a) in Moore *et al* (1998) in that all profiles are drawn to the formal force resolution. The straight lines indicate the slopes of two power laws: $\gamma = -1$ and $\gamma = -1.4$. The figure indeed shows that, at around 1% of the virial radius, the slope is steeper than -1 and the central slope increases as we increase the mass resolution. Moore *et al* (1998) interpreted this behaviour as evidence that the profiles are steeper than those predicted by the NFW profile. We also note that the results of our highest resolution run A₁ are qualitatively consistent with the results from Kravtsov *et al* (1999). Indeed, if the profiles are considered down to the scale of *two* formal resolutions, the density profile slope in the very central part of the profile $r \lesssim 0.01r_{\text{vir}}$ is close to $\gamma = -0.5$.

The profiles in figure 15.19 reflect the density distribution in the cores of simulated halos. However, the interpretation of these profiles is not straightforward because it requires an assessment of the numerical effects. The formal resolution does not usually even correspond to the scale where the numerical force is fully Newtonian (usually it is still considerably ‘softer’ than the Newtonian value). In the ART code, the inter-particle force reaches (on average) the Newtonian value at about two formal resolutions (see Kravtsov *et al* 1997). The effects of force resolution can be studied by re-simulating the same objects with higher force resolution and comparing the density profiles. Such a convergence study was done in Kravtsov *et al* (1998) where it was found that *for a fixed mass resolution* the halo density profiles converge at scales above two formal resolutions. Second, the local dynamical time for particles moving in the core of a halo is very short. For example, particles on the circular orbit of the radius $1h^{-1}$ kpc from the centre of halo A makes about 200 revolutions over the Hubble time. Therefore, if the time step is insufficiently small, numerical errors in these regions will tend to grow especially fast. The third possible source of numerical error is the mass resolution. Poor mass resolution in simulations with good force resolution may, for example, lead to two-body effects (e.g. Knebe *et al* 2000). An insufficient number of particles may also result in a ‘grainy’ potential in halo cores and thereby affect the accuracy of the orbit integration. In these effects, the mass resolution may be closely inter-related with the force resolution.

It is clear thus that, in order to draw conclusions unaffected by numerical errors, one has to determine the range of trustworthy scales using convergence analysis. The bottom panel in figure 15.19 shows that, for the halo A simulations, the convergence for vastly different mass and force resolution is reached for scales greater than or approximately equal to four formal force resolutions (all profiles in this figure are plotted down to the radius of four formal force resolutions). For all resolutions, there are more than 200 particles within the radius of four resolutions from the halo centre. For the highest resolution simulation (halo A₁) convergence is reached at scales $\gtrsim 0.005r_{\text{vir}}$.

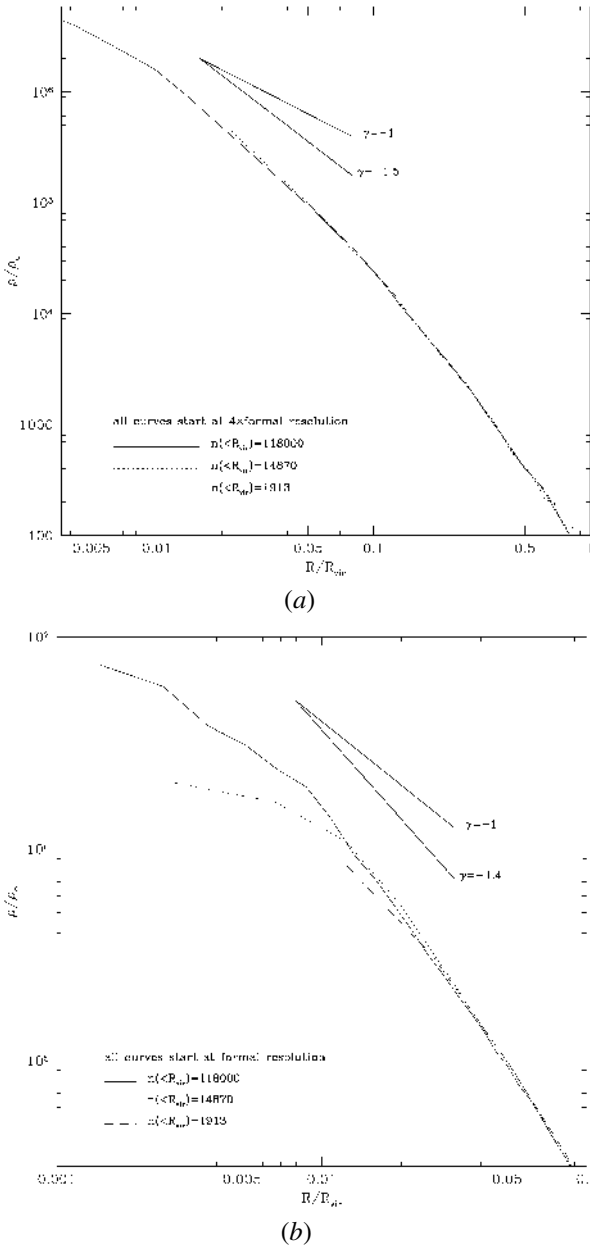


Figure 15.19. (a) Density profiles of halo A simulated with different mass and force resolutions. The profiles are plotted down to the formal force resolution of each simulation. (b) The profiles plotted down to *four formal resolutions*. It is clear that for vastly different mass (from 2000 to 120 000 particles in the halo) and force (from $3.66h^{-1}$ kpc to $0.23h^{-1}$ kpc) resolutions, convergence is reached at these scales.

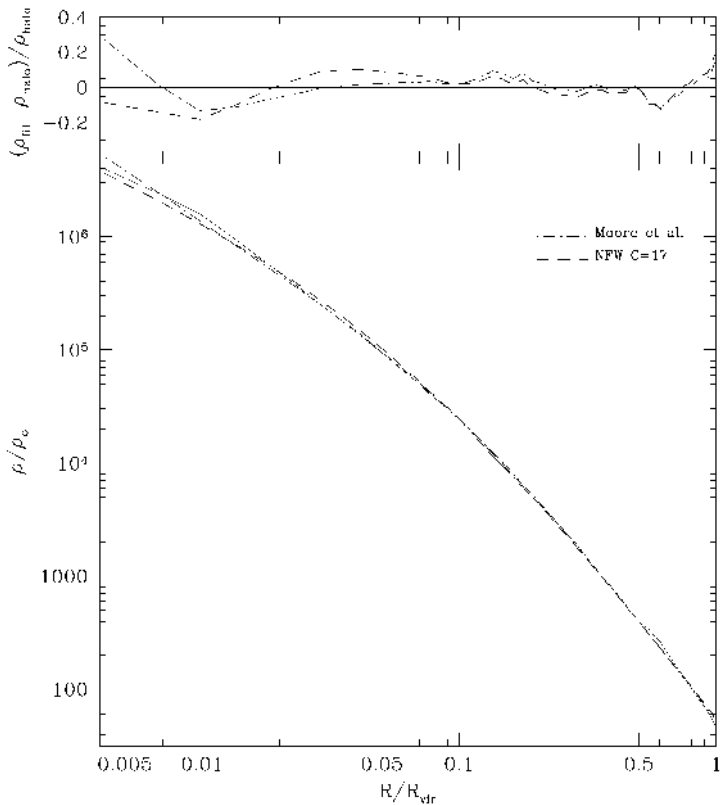


Figure 15.20. Fits of the NFW and Moore *et al* halo profiles to the profile of halo A₁ (*bottom panel*). The *top panel* shows the fractional deviations of the analytic fits from the numerical profile. Note that both analytical profiles fit the numerical profile equally well: fractional deviations are smaller than 20% over almost three decades in the radius.

In order to judge which profile provides a better description of the simulated profiles we fitted the NFW and Moore *et al* analytical profiles. Figure 15.20 presents the results of the fits and shows that both profiles fit the numerical profile equally well: fractional deviations of the fitted profiles from the numerical one are smaller than 20% over almost three decades in the radius. It is thus clear that the fact that the numerical profile has a slope steeper than -1 at the scale of $\sim 0.01 r_{\text{vir}}$ does not mean that a good fit of the NFW profile (or even analytical profiles with shallower asymptotic slopes) cannot be obtained.

There is certainly a certain degree of degeneracy in fitting various analytic profiles to the numerical results. Figure 15.21 illustrates this further by showing results of fitting profiles (full curves) of the form $\rho(r) \propto (r/r_0)^{-\gamma} [1 + (r/r_0)^\alpha]^{-(\beta-\alpha)/\gamma}$ to the same (halo A₁) simulated halo profile shown as full

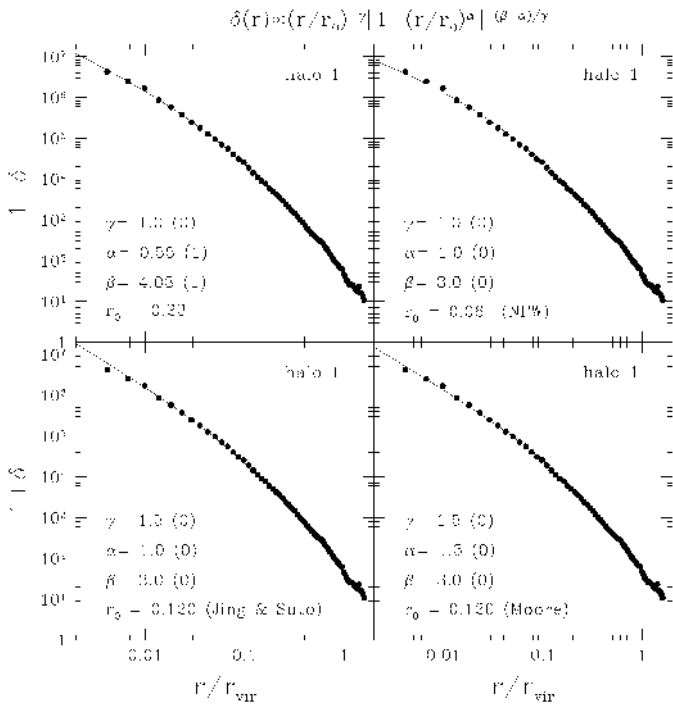


Figure 15.21. Analytical fits to the density profile of halo A1 (see table 15.4) from our set of simulations. The fits are of the form $\rho(r) \propto (r/r_0)^{-\gamma} [1 + (r/r_0)^\alpha]^{-(\beta-\alpha)/\gamma}$. The legend in each panel indicates the corresponding values of α , β and γ of the fit; the digit in parentheses indicates whether the parameter was kept fixed (0) or not (1) during the fit. Note that various sets of parameters, α , β , γ , provide equally good fits to the simulated halo profile in the whole resolved range of scales $\approx (0.005-1)r_{\text{vir}}$. This indicates a large degree of degeneracy in the parameters α , β and γ .

circles. The legend in each panel indicates the corresponding values of α , β and γ of the fit; the digit in parentheses indicates whether the parameter was kept fixed (0) or not (1) during the fit. The two right-hand panels show the fits of the NFW and Moore *et al* profiles; the bottom left-hand panel shows fit of the profiles used by Jing and Suto (2000). The top left-hand panel shows a fit in which the inner slope was fixed but α and β were fitted. The figure shows that all four analytic profiles can provide a nice fit to the numerical profile in the whole range $(0.005-1)r_{\text{vir}}$.

15.4.4.2 Halo profiles at $z = 1$

As we have mentioned, the halo A analysed in the previous section is somewhat special because it was selected as an isolated relaxed halo. In order to reach unbiased conclusions, in this section we will present an analysis of halos from the second set of simulations (halos B, C and D in table 15.4) which were not selected to be relaxed or isolated. Based on the results of the convergence study presented in the previous section, we will consider profiles of these halos only at scales above four formal resolutions using results starting only from four formal resolutions and not less than 200 particles. Note that these conditions are probably more stringent than necessary because these halos were simulated with five to seven times more particles per halo. There is an advantage in analysing halos at a relatively high redshift. Halos of a given mass will have a lower concentration (see Bullock *et al* 2001). A lower concentration implies a large scale at which the asymptotic inner slope is reached. Profiles of the high-redshift halos should, therefore, be more useful in discriminating between the analytic models with different inner slopes.

We found that a substantial substructure is present inside the virial radius in all three halos. Figure 15.22 shows the profiles of these halos at $z = 1$. There profiles are not as smooth as that of halo A₁ due to their substructure. Note that bumps and depressions visible in the profiles cannot have a significantly larger amplitude than the shot noise. Halo C appeared to be the most relaxed of the three halos. It also had its last major merger somewhat earlier than the other two. Halo D had a major merger event at $z \approx 2$. Remnants of the merger are still visible as a hump at radii around $100h^{-1}$ kpc. Non-uniformities in the profiles caused by the substructure may substantially bias the analytic fits to the entire range of scales below the virial radius. Therefore, we used only the central, presumably more relaxed, regions in the analytic fits: $r < 50h^{-1}$ kpc for halo D and $r < 100h^{-1}$ kpc for halos B and C (fits using only central $50h^{-1}$ kpc did not change the results).

The best-fit parameters were obtained by minimizing the maximum fractional deviation of the fit: $\max(\text{abs}(\log \rho_{\text{fit}}) - \log \rho_h)$. Minimizing the sum of the squares of deviations (χ^2), as is often done, can result in larger errors at small radii with the false impression that the fit fails because it has a wrong central slope. The fit that minimizes the maximum deviations improves the NFW fit for points in the range of radii $(5\text{--}20)h^{-1}$ kpc, where the NFW fit would appear to be below the data points if the fit was done by χ^2 minimization. This improvement comes at the expense of a few points around $1h^{-1}$ kpc. For example, if we fit halo B by using χ^2 minimization, the concentration decreases from 12.3 (see table 15.4) to 11.8. We also made a fit for halo B assuming even more stringent limits on the effects of numerical resolution. By minimizing the maximum deviation we fitted the halo starting at six times the formal resolution. Inside this radius there were about 900 particles. The resulting parameters of the fit were close to those in table 15.4: $C_{\text{NFW}} = 11.8$, and the maximum error of the NFW fit was 17%.

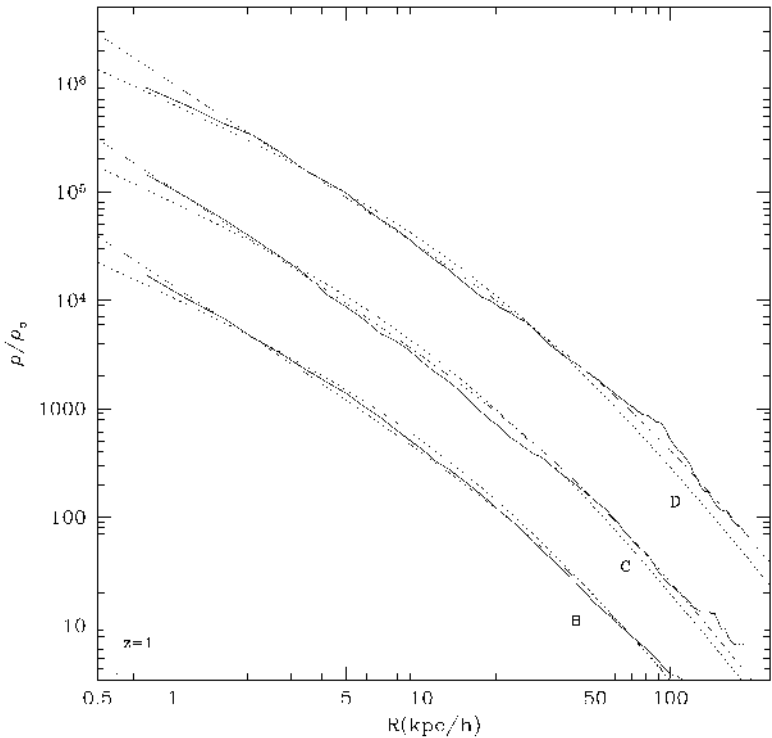


Figure 15.22. Profiles of halos B, C and D at $z = 1$. The profiles of halos C and D were offset downwards by factors of 10 and 100 for clarity. The full curves show simulated profiles, while the dotted and chain curves show the NFW and Moore *et al* fits, respectively. The halo profiles in the simulations are plotted down to four formal resolutions. Each halo had more than 200 particles inside the smallest plotted scale.

We found that the errors in the Moore *et al* fits were systematically smaller than those of the NFW fits, though the differences were not dramatic. The Moore *et al* fit failed for halo D. It formally gave very small errors, but this was done for a fit with an unreasonably small concentration ($C = 2$). When we constrained the approximation to have a concentration twice as large compared with the best NFW fit, we were able to obtain a reasonable fit (this fit is shown in figure 15.22). Nevertheless, the central part was fitted poorly in this case.

Our analysis therefore failed to determine which analytic profile provides a better description of the density distribution in simulated halos. Despite the larger number of particles per halo and lower concentrations of halos, the results are still inconclusive. The Moore *et al* profile is a better fit to the profile of halo C; the NFW profile is a better fit to the central part of halo D. Halo B represents

an intermediate case where both profiles provide equally good fits (similar to the analysis of halo A).

Note that there seems to be real deviations in the parameters of halos of the same mass. Halos B and D have the same virial radii and nearly the same circular velocities, yet their concentrations are different by 30%. We find the same differences in estimates of $C_{1/5}$ concentrations, which do not depend on the specifics of an analytic fit. The central slope at around 1 kpc also changes from halo to halo.

15.4.4.3 Summary

In this section we have given a review of some of the internal properties of DM halos focusing mostly on their profiles and concentrations. Our results are mostly based on simulations done with the ART code, which is capable of handling particles with different masses, variable force and time resolution. In runs with the highest resolution, the code achieved (formal) dynamical range of $2^{17} = 131\,072$ with 500 000 steps for particles at the highest level of resolution.

Our conclusions regarding the convergence of the profiles differ from those of Moore *et al* (1998). If we take into account only the radii, at which we believe the numerical effects (the force resolution, the resolution of initial perturbations and two-body scattering) to be small, then we find that the slope and amplitude of the density do not change when we change the force and mass resolution. This result is consistent with what was found in simulations of the ‘Santa Barbara’ cluster (Frenk *et al* 1999): at a fixed *resolved* scale the results do not change as the resolution increases. For the ART code the results converged at four times the formal force resolution and more than 200 particles. These convergence limits very likely depend on the particular code used and on the duration of the integration.

We reproduce Moore *et al*’s results regarding convergence and the results from Kravtsov *et al* (1998) regarding shallow central profiles, but only when we considered points inside unresolved scales. We conclude that those results followed from an overly optimistic interpretation of the numerical accuracy of the simulations.

For the galaxy-size halos considered in this section with masses $M_{\text{vir}} = 7 \times 10^{11} h^{-1} M_{\odot}$ to $2 \times 10^{12} h^{-1} M_{\odot}$ and concentrations $C = 9\text{--}17$ both the NFW profile, $\rho \propto r^{-1}(1+r)^{-2}$, and the Moore *et al* profile, $\rho \propto r^{-1.5}(1+r^{1.5})^{-1}$, give good fits with an accuracy of about 10% for radii not smaller than 1% of the virial radius. None of the profiles is significantly better than the other.

Halos with the same mass may have different profiles. No matter what profile is used—NFW or Moore *et al*—there is no universal profile: halo mass does not yet define the density profile. Nevertheless, the universal profile is an extremely useful notion which should be interpreted as the general trend $C(M)$ of halos with a larger mass to have a lower concentration. Deviations from the general $C(M)$ are real and significant (Bullock *et al* 2001). It is not yet clear but it seems very

likely that the central slopes of halos also have real fluctuations. The fluctuations in the concentration and central slopes are important for interpreting the central parts of rotation curves.

References

- Aarseth S J 1963 *Mon. Not. R. Astron. Soc.* **126** 223
 ——— 1985 *Multiple Time Scales* ed J W Brackbill and B J Cohen (New York: Academic Press) p 377
- Aarseth S J, Gott J R and Turner E L 1979 *Astrophys. J.* **228** 664
- Appel A 1985 *SIAM J. Sci. Stat. Comput.* **6** 85
- Avila-Reese *et al* 1999 *Mon. Not. R. Astron. Soc.* **310** 527
- Barnes J and Hut P 1986 *Nature* **324** 446
- Benson A J, Cole S, Frenk C S, Baugh C M and Lacey C D 2000 *Mon. Not. R. Astron. Soc.* **311** 793 (astro-ph/9903343)
- Bertschinger E 1998 *Annu. Rev. Astron. Astrophys.* **36** 599
 ——— 2001 *Preprint* astro-ph/0103301
- Bertschinger E and Gelb J 1991 *Comput. Phys.* **5** 164
- Binney J and Tremaine S 1987 *Galactic Dynamics* (Princeton, NJ: Princeton University Press)
- Bouchet F R and Hernquist L 1988 *Astrophys. J. Suppl.* **68** 521
- Bullock J S, Kolatt T S, Sigad Y, Somerville R S, Kravtsov A V, Klypin A, Primack J P and Dekel A 2001 *Mon. Not. R. Astron. Soc.* **321** 559 (astro-ph/9908159)
- Bullock J S, Kravtsov A V and Weinberg D H 2000 *Astrophys. J.* **539** 517 (astro-ph/0002214)
- Catelan P, Lucchin F, Matarrese S and Porciani C 1998a *Mon. Not. R. Astron. Soc.* **297** 692
- Catelan P, Matarrese S and Porciani C 1998b *Astrophys. J. Lett.* **502** 1
- Colín P, Klypin A and Kravtsov A 2000 *Astrophys. J.* **539** 561 (astro-ph/9907337)
- Colín P, Klypin A A, Kravtsov A V and Khokhlov A M 1999 *Astrophys. J.* **523** 32 (astro-ph/9809202)
- Couchman H M P 1991 *Astrophys. J.* **368** 23
- Davis M, Efstathiou G, Frenk C S and White S D M 1985 *Astrophys. J.* **292** 371
- Dekel A and Lahav O 1999 *Astrophys. J.* **520** 24 (astro-ph/9806193)
- Dekel A and Silk J 1986 *Astrophys. J.* **303** 39
- Diaferio A, Kauffmann G, Colberg J M and White S D M 1999 *Mon. Not. R. Astron. Soc.* **307** 537 (astro-ph/9812009)
- Doroshkevich A G, Kotok E V, Novikov I D, Polyudov A N and Sigov Yu S 1980 *Mon. Not. R. Astron. Soc.* **192** 321
- Efstathiou G, Davis M, Frenk C S and White S D M 1985 *Astrophys. J. Suppl.* **57** 241
- Flores R A and Primack J R 1994 *Astrophys. J.* **427** L1
- Frenk C *et al* 1999 *Astrophys. J.* **525** 630
- Gelb J 1992 *PhD Thesis* MIT
- Ghigna S, Moore B, Governato F, Lake G, Quinn T and Stadel J 1998 *Mon. Not. R. Astron. Soc.* **300** 146
 ——— *Observational Cosmology: The Development of Galaxy Systems* ed G Giuricin, M Mezzetti and P Solucci (San Francisco, CA: ASP) p 140
 ——— 2000 *Astrophys. J.* **544** 616